SIAM Review
Vol. 66, No. 3, pp. 501–532





# When Data Driven Reduced Order Modeling Meets Full Waveform Inversion*

Liliana Borcea†
Josselin Garnier‡
Alexander V. Mamonov§
Jörn Zimmerling¶

**Abstract.** Waveform inversion is concerned with estimating a heterogeneous medium, modeled by variable coefficients of wave equations, using sources that emit probing signals and receivers that record the generated waves. It is an old and intensively studied inverse problem with a wide range of applications, but the existing inversion methodologies are still far from satisfactory. The typical mathematical formulation is a nonlinear least squares data fit optimization and the difficulty stems from the nonconvexity of the objective function that displays numerous local minima at which local optimization approaches stagnate. This pathological behavior has at least three unavoidable causes: (1) The mapping from the unknown coefficients to the wave field is nonlinear and complicated. (2) The sources and receivers typically lie on a single side of the medium, so only backscattered waves are measured. (3) The probing signals are band limited and with high frequency content. There is a lot of activity in the computational science and engineering communities that seeks to mitigate the difficulty of estimating the medium by data fitting. In this paper we present a different point of view, based on reduced order models (ROMs) of two operators that control the wave propagation. The ROMs are called data driven because they are computed directly from the measurements, without any knowledge of the wave field inside the inaccessible medium. This computation is noniterative and uses standard numerical linear algebra methods. The resulting ROMs capture features of the physics of wave propagation in a complementary way and have surprisingly good approximation properties that facilitate waveform inversion.

**Key words.** inverse wave scattering, data driven, reduced order modeling, optimization

**MSC codes.** 65M32, 41A20

**DOI.** 10.1137/23M1552826

*Received by the editors February 13, 2023; accepted for publication (in revised form) January 8, 2024; published electronically August 8, 2024.
https://doi.org/10.1137/23M1552826

**Funding:** The work of the first and second authors was supported in part by the AFOSR award FA9550-22-1-0077. The work of the first and third authors was supported in part by U.S. Office of Naval Research award N00014-21-1-2370. The work of the second author was supported in part by Agence de l'Innovation de Défense (AID) via Centre Interdisciplinaire d'Etudes pour la Défense et la Sécurité (CIEDS, project PRODIPO). The work of the fourth author was supported in part by National Science Foundation grant 2110265.

†Department of Mathematics, University of Michigan, Ann Arbor, MI 48109-1043 USA (borcea@umich.edu).

‡CMAP, CNRS, Ecole Polytechnique, Institut Polytechnique de Paris, 91120 Palaiseau, France (josselin.garnier@polytechnique.edu).

§Department of Mathematics, University of Houston, Houston, TX 77204-3008 USA (avmamonov@uh.edu).

¶Uppsala Universitet, Department of Information Technology, Division of Scientific Computing, 75105 Uppsala, Sweden (jorn.zimmerling@it.uu.se).

**Contents**



**1. Introduction to Waveform Inversion. Paper Motivation and Outline.** The estimation of a heterogeneous medium from the time history of the wave field recorded at a few accessible locations is important in medical diagnostics via ultrasound, nondestructive evaluation of aging concrete in bridges and buildings, testing of aircraft fuselage, radar imaging, underwater acoustics, seismology, geophysical exploration, and so on. It is an inverse problem for a wave equation or a system of such equations (acoustic, electromagnetic, or elastic), where the heterogeneous medium is modeled by unknown variable coefficients. The goal is to determine these coefficients from measurements of the wave field, the solution of the wave equation, with forcing that is typically, but not always, controlled by the user.

To keep the presentation simple, we consider acoustic waves in a medium with constant mass density and unknown variable wave speed $c(\boldsymbol{x})$, a piecewise smooth, nonnegative, and bounded function. The wave field is modeled by the acoustic pressure $p(t,\boldsymbol{x})$, the solution of the wave equation

$$\left[\partial_t^2 - c^2(\boldsymbol{x})\Delta\right] p(t,\boldsymbol{x}) = S(t,\boldsymbol{x}), \qquad t \in \mathbb{R}, \quad \boldsymbol{x} \in \Omega \subset \mathbb{R}^d, \tag{1.1}$$

in dimension $d = 2$ or 3, with forcing $S(t, \boldsymbol{x})$ and homogeneous initial condition $p(t, \boldsymbol{x}) = 0$ at $t \ll 0$, i.e., at negative time, outside the temporal support of $S(t, \boldsymbol{x})$. We assume a bounded and simply connected domain $\Omega$ with smooth enough perfectly reflecting boundary $\partial\Omega$. This may be a real boundary of a closed cavity, but in general it is a fictitious boundary introduced for the convenience of the analysis and computations. Note that the waves propagate at finite speed, so if we place $\partial\Omega$ far enough from the spatial support of $S(t, \boldsymbol{x})$, there are no boundary effects over the finite duration of the data gathering experiment and we can choose any homogeneous boundary conditions.

The forcing in (1.1) is commonly controlled by the user and is modeled as a point source at $\boldsymbol{x}_s \in \Omega$ that emits a probing signal $f(t)$,

$$S(t, \boldsymbol{x}) = f(t)\delta_{\boldsymbol{x}_s}(\boldsymbol{x}), \tag{1.2}$$

where $\delta_{\boldsymbol{x}_s}(\boldsymbol{x})$ is the Dirac delta at $\boldsymbol{x}_s$. Typically, there are $m_s$ such sources, which probe the medium one at a time, so to keep track of the generated wave, the solution of (1.1) with right-hand side (1.2), we denote it by $p^{(s)}(t, \boldsymbol{x})$. The inverse problem is as follows: *Determine $c(\boldsymbol{x})$ from the measurements at receiver locations $\boldsymbol{y}_r$ for $r = 1, \ldots, m_r$, organized in the $m_r \times m_s$ time-dependent matrix $\boldsymbol{\mathcal{M}}(t)$ with entries*

$$\mathcal{M}_{r,s}(t) = p^{(s)}(t, \boldsymbol{y}_r), \qquad s = 1, \ldots, m_s, \quad r = 1, \ldots, m_r, \quad t \in (t_{\min}, t_{\max}). \tag{1.3}$$

The duration and frequency content of the probing signal matter and are application specific. The generic model of the emitted signal is $f(t) = B\varphi(Bt)\cos(\omega_o t)$, where $B\varphi(Bt)$ is an envelope function supported at $t \in [-1/B, 1/B]$ with Fourier transform $\widehat{\varphi}(\omega/B)$ that is large at angular frequency $\omega$ satisfying $|\omega| \leq O(B)$. Thus, $B$ is called the bandwidth. The modulation by the cosine shifts the frequency content of $f(t)$ to the intervals $|\omega \pm \omega_o| \leq O(B)$ according to the formula

$$\widehat{f}(\omega) = \int_{\mathbb{R}} dt\, f(t) e^{i\omega t} = \frac{1}{2}\left[\widehat{\varphi}\left(\frac{\omega - \omega_o}{B}\right) + \widehat{\varphi}\left(\frac{\omega + \omega_o}{B}\right)\right], \tag{1.4}$$

so $\omega_o$ is called the central frequency. Basic resolution studies suggest that signals with short $O(1/B)$ support and with high frequency content produce sharper estimates of the medium [27, 11]. This explains the wide use of pulses with modulation frequency $\omega_o \gg B$, but there are exceptions. In long-range imaging with radar [30], pulses are not used because sources have limited instantaneous power of emission and, due to geometrical spreading, the waves that reach the receivers are weaker than ambient noise. Chirped signals (long signals whose frequency increases with time) are used instead, because they allow an increase in the delivered net power and better signal-to-noise ratios. The inversion methodology with pulses or chirps is the same, due to the simple "pulse compression" data processing $f(-t) \star_t p^{(s)}(t, \boldsymbol{y}_r)$, where $f(-t)$ is the time-reversed emitted signal and $\star_t$ denotes time convolution [30]. Mathematically, by linearity of the wave equation, this processing is equivalent to working with the wave generated by the signal $F(t) = f(-t) \star_t f(t)$, which turns out to have much shorter duration than the chirp, i.e., it is a pulse [45].

We refer the interested reader to the mathematical literature on the uniqueness and stability of the inverse problem (see [8, 61, 50] and others). Many of these studies are for different types of data, like the Dirichlet to Neumann map, which are not available in the applications that we have in mind. Furthermore, uniqueness cannot be expected to hold in the strict sense, even in the best circumstances, because the

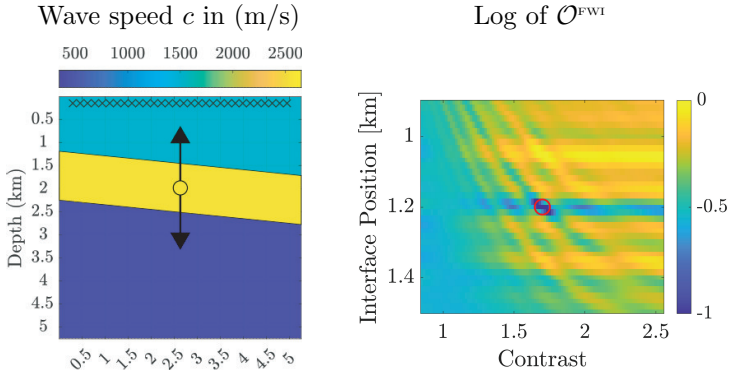


**Fig. 1.1** *Illustration of a two-parameter search for the true piecewise constant model $c(\boldsymbol{x})$ (left plot) in a closed rectangular cavity. The sources and receivers are colocated and shown as black $\times$. The probing signal contains frequencies in the interval $[2, 10]$Hz. The search parameters are the depth of the top left corner of the slanted fast layer (interface position), which varies over the range indicated by the black arrows, and the ratio of the wave speed inside and above the layer (contrast). The FWI objective function* (1.5) *is shown in the right plot. The true parameters are indicated by* ◯.

measurements are band limited: Variations of $c(\boldsymbol{x})$ on scales that are much smaller than the central wavelength cannot be determined. This issue is addressed in practice by a proper choice of the space $\mathcal{W}$ in which the search speed $w(\boldsymbol{x})$ lies and by adding a regularization penalty to the optimization.

The generic formulation of the inverse problem is a nonlinear least squares data fit optimization: $\min_{w\in\mathcal{W}} \mathcal{O}^{\rm FWI}(w) +$ regularization, with

$$\mathcal{O}^{\rm FWI}(w) = \sum_{r=1}^{m_r}\sum_{s=1}^{m_s}\int_{t_{\min}}^{t_{\max}} dt\,|\mathcal{M}_{r,s}(t) - p^{(s)}(t,\boldsymbol{y}_r;w)|^2. \tag{1.5}$$

Here $\boldsymbol{\mathcal{M}}(t)$ is the data matrix (1.3), $w(\boldsymbol{x}) \mapsto p^{(s)}(t,\boldsymbol{y}_r;w)$ is called the forward map, and $p^{(s)}(t,\boldsymbol{x};w)$ denotes the solution of the wave equation with wave speed $w(\boldsymbol{x})$. To avoid complicated notation, we omit the true wave speed from the list of arguments of the wave field and measurements. Thus, $p^{(s)}(t,\boldsymbol{x})$ is the pressure field for the true speed $c(\boldsymbol{x})$ and $p^{(s)}(t,\boldsymbol{x};w)$ is the pressure field for the search speed $w(\boldsymbol{x})$.

The optimization formulation defined by (1.5) has been coined by the acronym FWI (full waveform inversion) in the geophysics community [65]. The FWI formulation applies to an arbitrary data acquisition geometry, but the result of the inversion is strongly influenced by it. For example, it is easier to work with sources and receivers placed all around $\Omega$, so that both the waves transmitted through the medium and those that are backscattered can be measured. Unfortunately, the options for placing the sources and receivers are usually limited to one side of $\Omega$, so only the backscattered waves can be measured. It is well known that the FWI objective function (1.5) for such measurements exhibits numerous local minima at search speeds $w(\boldsymbol{x})$ that bear no relation to $c(\boldsymbol{x})$ [65]. See Figure 1.1 for an illustration. Any iterative local optimization method [44] applied to such an objective function will likely fail to obtain a good approximation of $c(\boldsymbol{x})$.

The pathological behavior of the FWI objective function seen in Figure 1.1 is called "cycle-skipping" and arises when the timing between the measured waves and those predicted by the forward model differs by more than half the cycle of oscillation.

The main causes are the complicated nonlinear forward mapping and the lack of low frequencies in the probing signal. Waves are backscattered by the rough part of $c(\boldsymbol{x})$, the "reflectivity," which corresponds to the jump discontinuities at the slanted layer in Figure 1.1. Reflections at these discontinuities and at the top boundary, located just above the sources/receivers, cause multiple arrivals (echoes) in the recorded data. When moving the layer up and down, the errors in the arrival times of these echoes exceed half a cycle, repeatedly, so we get the multiple horizontal stripes (highs and lows) in Figure 1.1. The smooth part of $c(\boldsymbol{x})$, the "kinematics," determines the travel time of the transmitted waves and is another cause of cycle-skipping in Figure 1.1. The curved stripes in the figure appear because when misestimating $c(\boldsymbol{x})$ inside the layer, we get wrong arrival times for the waves that penetrate there, scatter at the bottom of the layer, and then reach the receivers.

Cycle-skipping can sometimes be mitigated by adding prior information on $c(\boldsymbol{x})$ or by starting with a good initial guess. For the latter, the following observation is useful: It is easier to determine the kinematics from very low frequency data, because we can have larger errors for travel times that remain within the long cycle of oscillation [25, 65]. High frequencies are better for estimating the reflectivity if the kinematics is known and the multiple scattering effects are not too strong [62, 11]. This has motivated studies like [26, 22, 25] that obtain progressively better estimates of $c(\boldsymbol{x})$, starting from the lower frequencies. Unfortunately, low enough frequencies are rarely available and a reasonable initial guess does not guarantee success. Indeed, Figure 1.1 shows that cycle-skipping may occur even near the true $c(\boldsymbol{x})$.

The outstanding question is: How can we improve the objective function (1.5) so that numerically feasible local optimization methods can give good estimates of $c(\boldsymbol{x})$, irrespective of the starting point? One approach is to get rid of the $L^2([t_{\min}, t_{\max}])$ metric and replace it with a better one, such as the Wasserstein metric from optimal transport theory [35, 67]. The convexity of the data misfit function in this metric has been shown for a few simple models in [36, 58] and it holds for the example in Figure 1.1. However, later in this paper we will present another example in which convexity does not hold. Another approach, known as "modeling operator extension" [49] or "extended FWI" [64, 66], introduces in a systematic way additional degrees of freedom in the optimization and then drives the results toward a physically meaningful result. An explicit analysis of such a method, which minimizes the data misfit over both $c(\boldsymbol{x})$ and $f(t)$ in a very simple setting, can be found in [63]. There are various other ideas that have been tried, including machine learning [29, 31]. Nevertheless, the state of the field remains far from satisfactory and theoretical guarantees that any particular method will work even in simple settings are rare.

Our goal in this paper is to show that tools from reduced order modeling can be used to improve the waveform inversion methodology. Model order reduction is a popular topic in computational science, concerned mostly with reducing the computational complexity of a given dynamical system (the model) for purposes like design and control [2, 60, 9]. The idea is to obtain a low-dimensional, computationally inexpensive reduced order model (ROM) that approximates the response of the true model over a range of input parameters. In waveform inversion the model is defined by the wave equation, which we know, and the wave speed $c(\boldsymbol{x})$, which is unknown. Thus, we are interested in data driven ROMs that are computed directly from the measurements of the wave field, without knowing the wave speed model.

Data driven reduced order modeling is a rapidly growing field that combines ideas from optimization, numerical analysis, and projection based reduced order modeling.

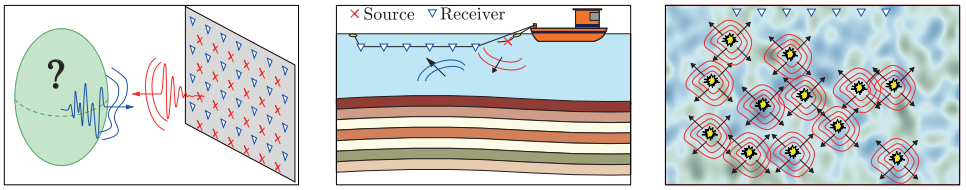


**Fig. 1.2** *Illustration of three data acquisition setups: With an active array (left), where the sources and receivers are colocated; with a towed-streamer (middle); with a passive array of receivers (blue triangles) and uncontrolled random sources (yellow) dispersed throughout the medium (right).*

Much of it is concerned with using a sparse set of "snapshots" of solutions of a time-dependent partial differential equation (PDE) to either learn the equation [23, 24] or approximate the time evolution of its solution [48, 47, 54, 55]. Both goals are of interest in waveform inversion, but none of these methods can be used because they assume knowledge of the snapshots at all points in $\Omega$.

The data driven ROMs used in this paper look like standard (reduced basis) projection ROMs [48, 23], because they are Galerkin projections of two operators related to $-c^2(\boldsymbol{x})\Delta$ on the space spanned by the snapshots $\{p^{(s)}(t_j,\boldsymbol{x}),\boldsymbol{x}\in\Omega\}_{s=1}^{m_s}$ at time instants $t_j$ for $j=0,\ldots,n-1$. However, there are fundamental differences:

1. The snapshots and therefore the approximation space are unknown. The ROMs can, however, be computed directly from the measurements $\boldsymbol{\mathcal{M}}(t)$.
2. The ROMs are matrices with structure designed to capture, at the algebraic level, the causal physics of wave propagation. They also have superior approximation properties that prove useful in inversion.

The starting point of our ROM construction is the mapping of the measurements $\boldsymbol{\mathcal{M}}(t)$ defined in (1.3) to a new data matrix $\boldsymbol{D}(t)$, whose components evaluated on the time grid $\{t_j\}_{j\geq 0}$ can be expressed as inner products of snapshots. The entries of the "mass" and "stiffness" matrices in the Galerkin approximations are determined by the same inner products, so they, and the ROMs, can be computed from $\boldsymbol{\mathcal{M}}(t)$. The mapping $\boldsymbol{\mathcal{M}}(t)\mapsto\boldsymbol{D}(t)$ can be carried out without any knowledge of $c(\boldsymbol{x})$, but it does require having colocated sources and receivers: $\boldsymbol{y}_s=\boldsymbol{x}_s$ for $s=1,\ldots,m_s=m_r=m$. We assume henceforth such a setup (see the left plot in Figure 1.2 for an illustration) and refer to the collection of sources/receivers as an "active array," which measures the "array response matrix" $\boldsymbol{\mathcal{M}}(t)$ defined in (1.3). This is an $m\times m$ symmetric matrix, due to source-receiver reciprocity.

Note that the active array setup is common in radar imaging and phased array ultrasonics, but it is not feasible in other fields, like geophysics. Nevertheless, there are data acquisition setups used in such fields in which it is possible to obtain a good approximation of the matrix $\boldsymbol{\mathcal{M}}(t)$ used by our construction. An example is the synthetic aperture, towed hydrophone streamer data acquisition used in marine seismic surveys (middle plot in Figure 1.2), where $\boldsymbol{\mathcal{M}}(t)$ is approximated using source-receiver reciprocity and interpolation, as explained in [20]. Another example, discussed later in the paper, considers opportunistic data acquisition setups with "passive arrays" of receivers, where the wave excitation comes from uncontrolled noise sources [42] (see the illustration in the right plot of Figure 1.2).

The presentation of our inversion methodology is organized in three sections.

Section 2 gives the data driven computation of two ROMs: The first ROM is for the "wave propagator operator," thus named because it propagates the wave field from

the instants $t_{j-1}$ and $t_j$ to the next instant $t_{j+1}$ for $j \geq 1$. It was first introduced in [32], where the resulting ROM was interpreted as a three-point spatial finite difference scheme on a special grid called "optimal." Such grids have been used in the past for obtaining superconvergent approximations of Neumann to Dirichlet maps [34, 4] and for solving various inverse problems [13, 14, 12]. However, the optimal grids are understood only in one dimension, which is why the results in [32] are limited to estimating the reflectivity of layered media. The extension of the propagator ROM to higher dimensions and its analysis that establishes the connection to Galerkin projections is given in [18], although the ROM had been used before in [16, 17, 33] for the purpose of imaging with waves, i.e., localizing the support of the reflectivity of a medium with known kinematics. The second ROM is for the operator $-c^2(\boldsymbol{x})\Delta$ and was introduced recently in [20]. We explain how the two ROMs are related, discuss their approximation properties, and compare them with the time domain reduced basis ROMs in the computational literature.

Section 3 is concerned with the use of the ROMs for waveform inversion. Roughly speaking, this involves the chain of maps $\boldsymbol{\mathcal{M}}(t) \mapsto \boldsymbol{D}(t) \mapsto \text{ROM} \mapsto$ estimate of $c(\boldsymbol{x})$, where the first two maps are those discussed in the previous section and the last map is computed using iterative optimization. We describe two distinct ideas for estimating $c(\boldsymbol{x})$: The first is to use a ROM estimate of the wave field inside $\Omega$, called the "estimated internal wave." This field depends on both the search and the true speeds, can be computed from the measurements, and can be used to linearize approximately the map $c(\boldsymbol{x}) \mapsto \boldsymbol{D}(t)$ [21]. Here we introduce a better use of the estimated internal wave, based on the observation that this wave fits the data, by construction, but unlike the true internal wave, it does not solve the wave equation. Thus, we estimate $c(\boldsymbol{x})$ by minimizing the residual in the wave equation. The second idea was introduced recently in [20] and minimizes the ROM misfit instead of the data misfit.

Section 4 gives the generalization of the inversion methodology to the opportunistic data acquisition setup with random sources.

We end with a few concluding remarks and open questions in section 5.

**2. The Data Driven ROMs.** The description of the computation of the ROMs involves four main steps: The first step, described in section 2.1, is the data mapping $\boldsymbol{\mathcal{M}}(t) \mapsto \boldsymbol{D}(t)$. The second step, described in section 2.2, defines the wave snapshots and the propagator operator that governs their evolution. The third step, given in section 2.3, introduces two Galerkin approximation schemes: one for the time stepping of the snapshots and one for the wave equation. The approximations are in an unknown space, but the Galerkin coefficients satisfy equations that are data driven. The fourth step, given in section 2.4, uses these equations to obtain our two ROMs. In section 2.5 we give a brief comparison of these ROMs to the standard (reduced basis) projection models found in the computational science literature. We end in section 2.6 with a brief discussion of regularization of the ROM computation.

**2.1. Data Transformation.** We will use functional calculus for a symmetrized wave operator. To define it, we must specify the boundary conditions. Any homogeneous boundary conditions that ensure a trivial kernel of the operator will do, so to fix ideas we consider henceforth the Dirichlet boundary conditions $p^{(s)}(t, \boldsymbol{x}) = 0$ at $\boldsymbol{x} \in \partial\Omega$. We assume that $c(\boldsymbol{x})$ equals the known constant $\bar{c}$ near the array, i.e., within the distance traveled by the waves during the short duration of the probing pulse $f(t)$. This assumption holds in most inversion setups and it simplifies the presentation. It is possible to extend the results to cases where it does not hold, but there are no

significant insights provided by such an extension.

The operator $-c^2(\boldsymbol{x})\Delta$ with homogeneous Dirichlet boundary conditions is positive definite and self-adjoint with respect to the inner product weighted by $c^{-2}(\boldsymbol{x})$. We prefer to work with the $L^2(\Omega)$ inner product, so we use the similarity transformation

$$p^{(s)}(t,\boldsymbol{x}) \mapsto P^{(s)}(t,\boldsymbol{x}) = \frac{\overline{c}}{c(\boldsymbol{x})} p^{(s)}(t,\boldsymbol{x}), \quad t \in \mathbb{R}, \quad \boldsymbol{x} \in \Omega, \tag{2.1}$$

which acts as the identity at the points in the array

$$P^{(s)}(t,\boldsymbol{x}_r) = p^{(s)}(t,\boldsymbol{x}_r) = \mathcal{M}_{r,s}(t), \qquad s,r = 1,\ldots,m. \tag{2.2}$$

The wave operator $\partial_t^2 - c^2(\boldsymbol{x})\Delta$ is transformed by (2.1) to $\partial_t^2 + \mathcal{A}$, where the operator $\mathcal{A} = -c(\boldsymbol{x})\Delta\,[c(\boldsymbol{x})\cdot]$ is positive definite and self-adjoint, with compact resolvent. Its spectrum [53, section 5.3] consists of a sequence of positive eigenvalues $\{\theta_j\}_{j\geq 1}$ and the eigenfunctions $\{y_j(\boldsymbol{x})\}_{j\geq 1}$ form an orthonormal basis of $L^2(\Omega)$. Functional calculus on $\mathcal{A}$ is defined as usual: If $\Phi : \mathbb{C} \mapsto \mathbb{C}$ is a continuous function, then $\Phi(\mathcal{A})$ is the self-adjoint operator with the same eigenfunctions as $\mathcal{A}$ and eigenvalues $\{\Phi(\theta_j)\}_{j\geq 1}$.

Our data mapping is stated in the next lemma. Its purpose is twofold: First, it gives a Duhamel-type principle, which maps the forcing in the wave equation to an initial condition. Second, it leads to an inner product expression of the entries of the data matrix, which is used in the computation of the ROMs.

LEMMA 1. *Define the new data matrix* $\boldsymbol{D}(t)$ *by the mapping*

$$\boldsymbol{\mathcal{M}}(t) \mapsto \boldsymbol{D}(t) = \boldsymbol{\mathcal{M}}^f(t) + \boldsymbol{\mathcal{M}}^f(-t), \quad \textit{with} \quad \boldsymbol{\mathcal{M}}^f(t) = -f'(-t) \star_t \boldsymbol{\mathcal{M}}(t), \tag{2.3}$$

*for* $t > 0$. *Its entries have the inner product expression*

$$D_{r,s}(t) = \int_\Omega d\boldsymbol{x}\, u_0^{(r)}(\boldsymbol{x}) u^{(s)}(t,\boldsymbol{x}), \quad \textit{with} \quad u^{(s)}(t,\boldsymbol{x}) = \cos\big(t\sqrt{\mathcal{A}}\big) u_0^{(s)}(\boldsymbol{x}), \tag{2.4}$$

*for* $r,s = 1,\ldots,m$. *Here* $u^{(s)}(t,\boldsymbol{x})$ *is the solution of the homogeneous wave equation*

$$(\partial_t^2 + \mathcal{A}) u^{(s)}(t,\boldsymbol{x}) = 0, \qquad t > 0, \quad \boldsymbol{x} \in \Omega, \tag{2.5}$$

*with initial state* $u^{(s)}(0,\boldsymbol{x}) = u_0^{(s)}(\boldsymbol{x}) = \Big|\widehat{f}\big(\sqrt{\mathcal{A}}\big)\Big| \delta_{\boldsymbol{x}_s}(\boldsymbol{x})$ *and* $\partial_t u^{(s)}(0,\boldsymbol{x}) = 0$.

*Proof.* The proof is given in [18, Appendix A], but we include it here, with more detailed explanation, for the convenience of the reader. Due to the convolution by $f'(-t)$ in (2.3), the $(r,s)$ entries of $\boldsymbol{\mathcal{M}}^f(t)$ are $\mathcal{M}^f_{r,s}(t) = P^{(s),f}(t,\boldsymbol{x}_r)$, where

$$P^{(s),f}(t,\boldsymbol{x}) = -f'(-t) \star_t P^{(s)}(t,\boldsymbol{x}) = F(t) \star_t H(t) \cos\big(t\sqrt{\mathcal{A}}\big) \delta_{\boldsymbol{x}_s}(\boldsymbol{x}) \tag{2.6}$$

solves the wave equation with forcing $F'(t)\delta_{\boldsymbol{x}_s}(\boldsymbol{x})$. Here, $F(t) = f(-t) \star_t f(t)$, $H(t)$ is the Heaviside step function, and the second term in the convolution is the time derivative of the causal Green's function of $\partial_t^2 + \mathcal{A}$. Functional calculus gives

$$\cos\big(t\sqrt{\mathcal{A}}\big)\delta_{\boldsymbol{x}_s}(\boldsymbol{x}) = \int_0^\infty d\theta\, \cos(t\sqrt{\theta}) \rho(\theta,\boldsymbol{x},\boldsymbol{x}_s), \tag{2.7}$$

where $\rho(\theta,\boldsymbol{x},\boldsymbol{x}_s) = \sum_{j\geq 1} \delta(\theta-\theta_j) y_j(\boldsymbol{x}_s) y_j(\boldsymbol{x})$ is the discrete spectral measure density associated with $\mathcal{A}$.

Substituting (2.7) into (2.6) and writing the convolution via the Fourier transform,

$$P^{(s),f}(t,\boldsymbol{x}) = \int_0^\infty d\theta \left[\frac{1}{2}\cos(t\sqrt{\theta})\widehat{F}(\sqrt{\theta}) + \int_{\mathbb{R}} \frac{d\omega}{2\pi}\frac{i\omega\widehat{F}(\omega)}{(\theta-\omega^2)}e^{-i\omega t}\right]\rho(\theta,\boldsymbol{x},\boldsymbol{x}_s). \tag{2.8}$$

The new $(r,s)$ data entries in (2.3) are $D_{r,s}(t) = P^{(s),f}(t,\boldsymbol{x}_r) + P^{(s),f}(-t,\boldsymbol{x}_r)$. The motivation for adding the negative $t$ term is that the even wave

$$P_e^{(s),f}(t,\boldsymbol{x}) = P^{(s),f}(t,\boldsymbol{x}) + P^{(s),f}(-t,\boldsymbol{x}) = \int_0^\infty d\theta\cos(t\sqrt{\theta})\widehat{F}(\sqrt{\theta})\rho(\theta,\boldsymbol{x},\boldsymbol{x}_s)$$

$$= \cos\big(t\sqrt{\mathcal{A}}\,\big)\widehat{F}\big(\sqrt{\mathcal{A}}\,\big)\delta_{\boldsymbol{x}_s}(\boldsymbol{x}), \qquad t>0, \quad \boldsymbol{x}\in\Omega, \tag{2.9}$$

has a simpler expression than (2.8), because

$$\int_{\mathbb{R}} \frac{d\omega}{2\pi}\frac{\omega\widehat{F}(\omega)}{(\theta-\omega^2)}\left(e^{-i\omega t}+e^{i\omega t}\right) = \int_{\mathbb{R}}\frac{d\omega}{\pi}\frac{\omega|\widehat{f}(\omega)|^2}{(\theta-\omega^2)}\cos(\omega t) = 0.$$

Moreover, (2.9) solves the homogeneous wave equation (2.5) with initial condition

$$P_e^{(s),f}(0,\boldsymbol{x}) = \widehat{F}\big(\sqrt{\mathcal{A}}\,\big)\delta_{\boldsymbol{x}_s}(\boldsymbol{x}), \qquad \partial_t P_e^{(s),f}(0,\boldsymbol{x}) = 0.$$

It remains to connect (2.9) to the wave defined in (2.4). To do so, we take the square root of $\widehat{F}(\omega) = |\widehat{f}(\omega)|^2$ and use the fact that functions of $\mathcal{A}$ commute. We find that

$$P_e^{(s),f}(t,\boldsymbol{x}) = \left|\widehat{f}\big(\sqrt{\mathcal{A}}\,\big)\right|\cos\big(t\sqrt{\mathcal{A}}\,\big)\left|\widehat{f}\big(\sqrt{\mathcal{A}}\,\big)\right|\delta_{\boldsymbol{x}_s}(\boldsymbol{x}) = \left|\widehat{f}\big(\sqrt{\mathcal{A}}\,\big)\right|u^{(s)}(t,\boldsymbol{x}) \tag{2.10}$$

for $t>0$ and $\boldsymbol{x}\in\Omega$. The statement of the lemma follows after substituting (2.10) into the expression of $D_{r,s}(t)$ and using the fact that $\mathcal{A}$ is self-adjoint:

$$D_{r,s}(t) = P_e^{(s),f}(t,\boldsymbol{x}_r) = \int_\Omega d\boldsymbol{x}\,\delta_{\boldsymbol{x}_r}(\boldsymbol{x})\left|\widehat{f}\big(\sqrt{\mathcal{A}}\,\big)\right|u^{(s)}(t,\boldsymbol{x}) \tag{2.11}$$

$$= \int_\Omega d\boldsymbol{x}\,\left|\widehat{f}\big(\sqrt{\mathcal{A}}\,\big)\right|\delta_{\boldsymbol{x}_r}(\boldsymbol{x})u^{(s)}(t,\boldsymbol{x}) = \int_\Omega d\boldsymbol{x}\,u_0^{(r)}(\boldsymbol{x})u^{(s)}(t,\boldsymbol{x}). \tag{2.12}$$

∎

Note that the transformation (2.3) can be carried out without any knowledge of the medium if the measurements start at $t_{\min} = -t_F$ (or earlier), where $(-t_F,t_F)$ is the support of $F(t)$. If the measurements start later, at $t_{\min} > -t_F$, we need the assumption that $c(\boldsymbol{x}) = \bar{c}$ near the array to compute the missing measurements in the interval $(-t_F,t_{\min})$. Near means within the distance $\bar{c}(t_{\min}+t_F)$ of the sources/receivers.

**2.2. The Snapshots and the Propagator.** To define the ROMs, we will use the snapshots of the wave (2.4) on a time grid with step $\tau$. The choice of $\tau$ matters, as explained in [19, section 6 and Appendix A] and in [21, 20]. For our purpose, it suffices to say that it should be $\tau\sim 2\pi/\omega_o$, where $\sim$ means equal, up to a finite constant. A larger $\tau$ does not sample the wave field according to the Nyquist criterion and gives poor approximation properties of the ROM. A smaller $\tau$ leads to poor conditioning of the mass matrix defined below and requires regularization. We comment briefly on regularization in section 2.6. More details are given in [20, Appendix E].

Let us gather the snapshots for all the $m$ sources in the row vector fields,

$$\boldsymbol{u}_j(\boldsymbol{x}) = \left(u^{(1)}(j\tau,\boldsymbol{x}),\dots,u^{(m)}(j\tau,\boldsymbol{x})\right), \qquad j\geq 0, \quad \boldsymbol{x}\in\Omega, \tag{2.13}$$

called henceforth the "vector snapshots." According to (2.4), they are given by

$$\boldsymbol{u}_j(\boldsymbol{x}) = \cos\big(j\tau\sqrt{\mathcal{A}}\,\big)\boldsymbol{u}_0(\boldsymbol{x}), \qquad j \geq 0, \quad \boldsymbol{x} \in \Omega, \tag{2.14}$$

and thanks to the trigonometric identity $\cos[(j+1)\alpha]+\cos[|j-1|\alpha] = 2\cos(\alpha)\cos(j\alpha)$ $\forall \alpha \in \mathbb{R}$, they satisfy the exact time stepping scheme

$$\boldsymbol{u}_{j+1}(\boldsymbol{x}) = 2\mathcal{P}\boldsymbol{u}_j(\boldsymbol{x}) - \boldsymbol{u}_{|j-1|}(\boldsymbol{x}), \qquad \mathcal{P} = \cos\big(\tau\sqrt{\mathcal{A}}\,\big), \tag{2.15}$$

for $j \geq 0$ and $\boldsymbol{x} \in \Omega$, driven by the propagator operator $\mathcal{P}$.

The ROMs will be computed from the $m \times m$ data matrices $\boldsymbol{D}_j = \boldsymbol{D}(j\tau)$, defined as in (2.3) and evaluated at the time instants $t_j = j\tau$ for $j = 0, \ldots, 2n-1$. According to Lemma 1, these have the integral expression

$$\boldsymbol{D}_j = \int_\Omega d\boldsymbol{x}\, \boldsymbol{u}_0^T(\boldsymbol{x})\boldsymbol{u}_j(\boldsymbol{x}) = \int_\Omega d\boldsymbol{x}\, \boldsymbol{u}_0^T(\boldsymbol{x}) \cos\big(j\tau\sqrt{\mathcal{A}}\,\big)\boldsymbol{u}_0(\boldsymbol{x}), \tag{2.16}$$

with kernel given by the Chebyshev polynomial $T_j$ of the first kind of the propagator operator: $\cos(j\tau\sqrt{\mathcal{A}}\,) = \cos(j \arccos \mathcal{P}) = T_j(\mathcal{P})$.

**2.3. Data Driven Galerkin Approximations.** We consider two Galerkin approximations of wave propagation in the finite-dimensional subspace $\mathscr{U}$ of $L^2(\Omega)$ generated by the $nm$ snapshots (for all $m$ sources and $n$ time instants):

$$\mathscr{U} = \text{range}\Big\{(u^{(s)}(j\tau, \boldsymbol{x}))_{\boldsymbol{x}\in\Omega},\, j = 0, \ldots, n-1,\, s = 1, \ldots, m\Big\}. \tag{2.17}$$

We assume that $\dim(\mathscr{U}) = nm$. This holds in general if $\tau \sim 2\pi/\omega_o$ and the separation between the sources is $\sim 2\pi\bar{c}/\omega_o$. If the dimension of $\mathscr{U}$ is smaller than $nm$, then the ROM construction requires regularization (section 2.6 and [20, Appendix E]).

Let us denote by $\boldsymbol{U}(\boldsymbol{x}) = \big(\boldsymbol{u}_0(\boldsymbol{x}), \ldots, \boldsymbol{u}_{n-1}(\boldsymbol{x})\big)$ the $nm$-dimensional row vector field that contains all the snapshots. The first Galerkin approximation is for the time stepping equation (2.15). It approximates the vector snapshots (2.13) by

$$\boldsymbol{u}_j^{\text{Gal}}(\boldsymbol{x}) = \boldsymbol{U}(\boldsymbol{x})\boldsymbol{g}_j, \qquad j \geq 0, \quad \boldsymbol{x} \in \Omega, \tag{2.18}$$

using the Galerkin coefficient matrices $\boldsymbol{g}_j \in \mathbb{R}^{nm\times m}$ defined so that the residual is orthogonal to the space $\mathscr{U}$. To write this explicitly, we use an orthonormal basis of $\mathscr{U}$, stored in the $nm$-dimensional row vector field

$$\boldsymbol{V}(\boldsymbol{x}) = \big(\boldsymbol{v}_0(\boldsymbol{x}), \ldots, \boldsymbol{v}_{n-1}(\boldsymbol{x})\big), \quad \boldsymbol{x} \in \Omega, \quad \text{with} \quad \int_\Omega d\boldsymbol{x}\, \boldsymbol{V}^T(\boldsymbol{x})\boldsymbol{V}(\boldsymbol{x}) = \boldsymbol{I}_{nm}. \tag{2.19}$$

Here $\boldsymbol{I}_{nm}$ is the $nm \times nm$ identity matrix. As we did for $\boldsymbol{U}(\boldsymbol{x})$, we organize the entries of $\boldsymbol{V}(\boldsymbol{x})$ in the $m$-dimensional row vectors $\boldsymbol{v}_j(\boldsymbol{x})$ associated with the instants $j\tau$ for $j = 0, \ldots, n-1$. This makes sense because our basis has the "causal" property

$$(\boldsymbol{v}_j(\boldsymbol{x}))_{\boldsymbol{x}\in\Omega} \in \text{range}\,\{(\boldsymbol{u}_{j'}(\boldsymbol{x}))_{\boldsymbol{x}\in\Omega},\, j' = 0, \ldots, j\} \quad \text{for } j = 0, \ldots, n-1. \tag{2.20}$$

It is obtained by the Gram–Schmidt orthogonalization of the components of $\boldsymbol{U}(\boldsymbol{x})$,

$$\boldsymbol{U}(\boldsymbol{x}) = \boldsymbol{V}(\boldsymbol{x})\boldsymbol{R}, \qquad \boldsymbol{x} \in \Omega, \tag{2.21}$$

where $\boldsymbol{R}$ is an invertible $nm \times nm$ matrix with block upper triangular structure.

The orthogonality of the residual to $\mathscr{U}$ can now be written as

$$\int_\Omega d\boldsymbol{x}\, \boldsymbol{V}^T(\boldsymbol{x}) \left[\boldsymbol{U}(\boldsymbol{x})\boldsymbol{g}_{j+1} + \boldsymbol{U}(\boldsymbol{x})\boldsymbol{g}_{|j-1|} - 2\mathcal{P}\boldsymbol{U}(\boldsymbol{x})\boldsymbol{g}_j\right] = \boldsymbol{0} \qquad \forall j \geq 0, \tag{2.22}$$

and solving for $\boldsymbol{V}(\boldsymbol{x})$ from (2.21) we get the following time stepping scheme for the Galerkin coefficients:

$$\boldsymbol{R}^{-T}\left[\boldsymbol{M}(\boldsymbol{g}_{j+1} + \boldsymbol{g}_{|j-1|}) - 2\boldsymbol{S}\boldsymbol{g}_j\right] = 0, \qquad j \geq 0. \tag{2.23}$$

Here $\boldsymbol{R}^{-T}$ denotes the transpose of $\boldsymbol{R}^{-1}$ and $\boldsymbol{M}$ and $\boldsymbol{S}$ are the $nm \times nm$ "mass" (Gramian) and "stiffness" matrices

$$\boldsymbol{M} = \int_\Omega d\boldsymbol{x}\, \boldsymbol{U}^T(\boldsymbol{x})\boldsymbol{U}(\boldsymbol{x}), \qquad \boldsymbol{S} = \int_\Omega d\boldsymbol{x}\, \boldsymbol{U}^T(\boldsymbol{x})\mathcal{P}\boldsymbol{U}(\boldsymbol{x}). \tag{2.24}$$

The second Galerkin approximation is for the wave equation (2.5). To distinguish it from the first, we use the tilde in the notation of the approximate wave field,

$$\widetilde{\boldsymbol{u}}^{\mathrm{Gal}}(t,\boldsymbol{x}) = \boldsymbol{U}(\boldsymbol{x})\widetilde{\boldsymbol{g}}(t), \qquad t \geq 0, \quad \boldsymbol{x} \in \Omega, \tag{2.25}$$

where the Galerkin coefficients $\widetilde{\boldsymbol{g}}(t)$ are $nm \times m$ time dependent matrices. These are defined so that when substituting (2.25) into the wave equation (2.5), the residual is orthogonal to the space $\mathscr{U}$, i.e.,

$$\int_\Omega d\boldsymbol{x}\, \boldsymbol{V}^T(\boldsymbol{x}) \left[\boldsymbol{U}(\boldsymbol{x})\widetilde{\boldsymbol{g}}''(t) + \mathcal{A}\boldsymbol{U}(\boldsymbol{x})\widetilde{\boldsymbol{g}}(t)\right] = \boldsymbol{0}, \qquad t \geq 0, \tag{2.26}$$

where $\widetilde{\boldsymbol{g}}''(t)$ denotes the second derivative of $\widetilde{\boldsymbol{g}}(t)$. Using (2.21) again, we obtain the semidiscretized wave equation in the Galerkin framework

$$\boldsymbol{R}^{-T}\left[\boldsymbol{M}\widetilde{\boldsymbol{g}}''(t) + \widetilde{\boldsymbol{S}}\widetilde{\boldsymbol{g}}(t)\right] = \boldsymbol{0}, \qquad t \geq 0, \tag{2.27}$$

where the mass matrix $\boldsymbol{M}$ is the same as in (2.24), but the stiffness matrix is

$$\widetilde{\boldsymbol{S}} = \int_\Omega d\boldsymbol{x}\, \boldsymbol{U}^T(\boldsymbol{x})\mathcal{A}\boldsymbol{U}(\boldsymbol{x}). \tag{2.28}$$

The Galerkin approximations described above are standard, except for the multiplication by $\boldsymbol{R}^{-T}$ of (2.23) and (2.27). Since $\boldsymbol{R}$ is nonsingular,[1] this multiplication does not change the solution of these equations. We only use it to obtain a good algebraic structure of our ROMs, as explained in the next section. The question is, how can we use these Galerkin approximations when we do not know the snapshots in $\boldsymbol{U}(\boldsymbol{x})$? The next two theorems show that, in fact, (2.23) and (2.27) are array data driven.

THEOREM 1. *Let $\boldsymbol{e}_j$ denote the $nm \times m$ column blocks of the identity matrix, i.e., $\boldsymbol{I}_{nm} = \big(\boldsymbol{e}_0, \boldsymbol{e}_1, \ldots, \boldsymbol{e}_{n-1}\big)$. The Galerkin coefficients in approximation* (2.18) *satisfy*

$$\boldsymbol{g}_j = \boldsymbol{e}_j, \qquad j = 0, \ldots, n-1. \tag{2.29}$$

[1] Recall that here we assume linearly independent snapshots, i.e., $\dim(\mathscr{U}) = nm$. Otherwise, we use regularization to obtain an invertible approximation of $\boldsymbol{R}$, as explained in section 2.6.

*The $m \times m$ blocks of the mass and stiffness matrices defined in* (2.24) *are given by the first $2n-1$ data matrices* (2.16) *as follows:*

$$\boldsymbol{M}_{i,j} = \int_\Omega d\boldsymbol{x}\, \boldsymbol{u}_i^T(\boldsymbol{x})\boldsymbol{u}_j(\boldsymbol{x}) = \frac{1}{2}\big(\boldsymbol{D}_{i+j} + \boldsymbol{D}_{|i-j|}\big), \tag{2.30}$$

$$\boldsymbol{S}_{i,j} = \int_\Omega d\boldsymbol{x}\, \boldsymbol{u}_i^T(\boldsymbol{x})\mathcal{P}\boldsymbol{u}_j(\boldsymbol{x}) = \frac{1}{4}\big(\boldsymbol{D}_{i+j+1} + \boldsymbol{D}_{|i-j+1|} + \boldsymbol{D}_{|i+j-1|} + \boldsymbol{D}_{|i-j-1|}\big) \tag{2.31}$$

*for $i, j = 0, \ldots, n-1$. The orthonormal basis $\boldsymbol{V}(\boldsymbol{x})$ cannot be computed without knowing $\boldsymbol{U}(\boldsymbol{x})$, but the block upper triangular matrix $\boldsymbol{R}$ in its definition* (2.21) *is data driven. It is the block Cholesky factor of the mass matrix: $\boldsymbol{R}^T\boldsymbol{R} = \boldsymbol{M}$.*

Note that there is an ambiguity in the definition of the block Cholesky factorization. The difference between various factorization algorithms is in the computation of the diagonal blocks of $\boldsymbol{R}$, which involves taking the square root of a symmetric, positive definite $m \times m$ matrix. Any algorithm will do, as long as it is used consistently throughout the inversion procedure. We use [16, Algorithm 5.2], which takes the square root using the spectral decomposition.

*Proof of Theorem* 1. Equation (2.29) seems natural, because the first $n$ snapshots define the approximation space. However, for the result to hold, we also need that these snapshots exactly satisfy the time stepping equation, which is indeed the case. The proof of (2.29) is as follows: Since $\dim(\mathscr{U}) = nm$, the matrices $\boldsymbol{R}$ and $\boldsymbol{M}$ are nonsingular. The definition of $\boldsymbol{U}(\boldsymbol{x})$ and (2.15) give that, if (2.29) holds, then the residual is

$$\begin{aligned}\boldsymbol{U}(\boldsymbol{x})(\boldsymbol{g}_{j+1} + \boldsymbol{g}_{|j-1|}) - 2\mathcal{P}\boldsymbol{U}(\boldsymbol{x})\boldsymbol{g}_j &= \boldsymbol{U}(\boldsymbol{x})(\boldsymbol{e}_{j+1} + \boldsymbol{e}_{|j-1|}) - 2\mathcal{P}\boldsymbol{U}(\boldsymbol{x})\boldsymbol{e}_j \\ &= \boldsymbol{u}_{j+1}(\boldsymbol{x}) + \boldsymbol{u}_{|j-1|}(\boldsymbol{x}) - 2\mathcal{P}\boldsymbol{u}_j(\boldsymbol{x}) = 0\end{aligned}$$

for $j = 0, \ldots, n-1$. Obviously, this residual satisfies (2.22), which is equivalent to (2.23). But (2.23) with initial conditions $\boldsymbol{g}_0 = \boldsymbol{e}_0$ and $\boldsymbol{g}_{-1} = \boldsymbol{g}_1$ has a unique solution, since $\boldsymbol{R}^{-T}\boldsymbol{M}$ is invertible, so the Galerkin coefficients must satisfy (2.29). Note that we use these initial conditions to ensure that the Galerkin approximation is exact at $t = 0$ and that it is even in time.

To prove (2.30), we use the expression (2.14) of the snapshots in the definition of the $(i, j)$ block of $\boldsymbol{M}$,

$$\begin{aligned}\boldsymbol{M}_{i,j} &= \int_\Omega d\boldsymbol{x}\, \Big\{\cos\big(i\tau\sqrt{\mathcal{A}}\,\big)\boldsymbol{u}_0(\boldsymbol{x})\Big\}^T \cos\big(j\tau\sqrt{\mathcal{A}}\,\big)\boldsymbol{u}_0(\boldsymbol{x}) \\ &= \int_\Omega d\boldsymbol{x}\, \boldsymbol{u}_0^T(\boldsymbol{x}) \cos\big(i\tau\sqrt{\mathcal{A}}\,\big) \cos\big(j\tau\sqrt{\mathcal{A}}\,\big)\boldsymbol{u}_0(\boldsymbol{x}) \\ &= \int_\Omega d\boldsymbol{x}\, \boldsymbol{u}_0^T(\boldsymbol{x}) \frac{1}{2}\Big\{\cos\big[(i+j)\tau\sqrt{\mathcal{A}}\,\big] + \cos\big[|i-j|\tau\sqrt{\mathcal{A}}\,\big]\Big\}\boldsymbol{u}_0(\boldsymbol{x}),\end{aligned}$$

where the second equality holds because $\mathcal{A}$ is self-adjoint and the last equality is by the trigonometric identity: $2\cos(i\alpha)\cos(j\alpha) = \cos\big[(i+j)\alpha\big] + \cos\big[|i-j|\alpha\big]$ $\forall\, \alpha \in \mathbb{R}$. The result (2.30) follows from (2.16).

The calculation of $\boldsymbol{S}$ is similar, because the time stepping scheme gives

$$\mathcal{P}\boldsymbol{u}_j(\boldsymbol{x}) = \frac{1}{2}\big[\boldsymbol{u}_{j+1}(\boldsymbol{x}) + \boldsymbol{u}_{|j-1|}(\boldsymbol{x})\big], \qquad j \geq 0, \quad \boldsymbol{x} \in \Omega.$$

Substituting this into the definition of $\boldsymbol{S}_{i,j}$ and using the calculation above, we get (2.31). Finally, we deduce from the Gram–Schmidt orthogonalization (2.21) and the definition (2.24) of the mass matrix that

$$\boldsymbol{M} = \int_\Omega d\boldsymbol{x}\, \boldsymbol{U}^T(\boldsymbol{x})\boldsymbol{U}(\boldsymbol{x}) = \boldsymbol{R}^T \int_\Omega d\boldsymbol{x}\, \boldsymbol{V}^T(\boldsymbol{x})\boldsymbol{V}(\boldsymbol{x})\boldsymbol{R} = \boldsymbol{R}^T\boldsymbol{R}. \tag{2.32}$$

∎

The second Galerkin approximation is on the same space $\mathscr{U}$, using the same basis in $\boldsymbol{V}(\boldsymbol{x})$ and the same mass matrix $\boldsymbol{M}$. The next theorem describes the other terms in the semidiscrete wave equation (2.27).

THEOREM 2. *The time dependent Galerkin coefficients in the approximation* (2.25) *satisfy the initial conditions*

$$\widetilde{\boldsymbol{g}}(0) = \boldsymbol{e}_0, \qquad \widetilde{\boldsymbol{g}}'(0) = \boldsymbol{0}. \tag{2.33}$$

*The $m \times m$ blocks of the stiffness matrix $\widetilde{\boldsymbol{S}}$ are given by*

$$\widetilde{\boldsymbol{S}}_{i,j} = \int_\Omega d\boldsymbol{x}\, \boldsymbol{u}_i^T(\boldsymbol{x})\mathcal{A}\boldsymbol{u}_j(\boldsymbol{x}) = -\frac{1}{2}\left[\ddot{\boldsymbol{D}}_{i+j} + \ddot{\boldsymbol{D}}_{|i-j|}\right], \qquad i,j = 0,\dots,n-1, \tag{2.34}$$

*where $\ddot{\boldsymbol{D}}_j$ denotes the second derivative of $\boldsymbol{D}(t)$ evaluated at $t = j\tau$.*

*Proof.* Equation (2.33) ensures that the Galerkin approximation (2.25) satisfies exactly the initial conditions

$$\widetilde{\boldsymbol{u}}^{\mathrm{Gal}}(0,\boldsymbol{x}) = \boldsymbol{U}(\boldsymbol{x})\boldsymbol{e}_0 = \boldsymbol{u}_0(\boldsymbol{x}), \quad \partial_t\widetilde{\boldsymbol{u}}^{\mathrm{Gal}}(0,\boldsymbol{x}) = \boldsymbol{U}(\boldsymbol{x})\widetilde{\boldsymbol{g}}'(0) = \boldsymbol{0}, \qquad \boldsymbol{x} \in \Omega. \tag{2.35}$$

The expression (2.34) of the stiffness matrix follows from the wave equation

$$\partial_t^2\boldsymbol{u}(t = j\tau, \boldsymbol{x}) = -\mathcal{A}\boldsymbol{u}_j(\boldsymbol{x}) \qquad \forall j \geq 0, \quad \boldsymbol{x} \in \Omega,$$

and the definition of $\boldsymbol{D}(t)$ given in Lemma 1. ∎

**2.4. The Data Driven ROMs.** We are now ready to define our two ROMs from the data driven Galerkin equations (2.23) and (2.27).

**2.4.1. The ROM Propagator.** This ROM is derived from (2.23) and defines a discrete time dynamical system, with state at time instant $t_j = j\tau$ given by the $j$th ROM snapshot, which is the $nm \times m$ matrix

$$\boldsymbol{u}_j^{\mathrm{ROM}} = \int_\Omega d\boldsymbol{x}\, \boldsymbol{V}^T(\boldsymbol{x})\boldsymbol{u}_j^{\mathrm{Gal}}(\boldsymbol{x}) = \int_\Omega d\boldsymbol{x}\, \boldsymbol{V}^T(\boldsymbol{x})\boldsymbol{U}(\boldsymbol{x})\boldsymbol{g}_j = \boldsymbol{R}\boldsymbol{g}_j, \qquad j \geq 0. \tag{2.36}$$

The second equality in this equation is by definition (2.18), and the third is due to the Gram–Schmidt equation (2.21). The ROM snapshots are data driven: The first $n$ of them are just the $nm \times m$ block columns of $\boldsymbol{R}$ due to (2.29),

$$\boldsymbol{u}_j^{\mathrm{ROM}} = \boldsymbol{R}\boldsymbol{e}_j, \qquad j = 0,\dots,n-1. \tag{2.37}$$

The others are obtained by time stepping in (2.23) for $j \geq n-1$.

REMARK 2.1. *The first ROM snapshot has nonzero entries only in the first $m \times m$ block. This is the algebraic way of capturing that $\boldsymbol{u}(t = 0, \boldsymbol{x})$ is supported near the array. As $j$ increases, the row blocks of $\boldsymbol{u}_j^{ROM}$ fill in sequentially, thus capturing the progressive advancement of the wave away from the array. This physical interpretation*

*is easier to visualize in the one-dimensional case, where we can transform the space coordinate to time using the travel time map* $x \mapsto \int_0^x dx'/c(x')$. *We work in higher dimensions, where such a travel time transformation cannot be done. Nevertheless, the interpretation remains formally true, in the sense that we can associate to each instant* $j\tau$ *a maximum "depth coordinate" reached by the wave, while the dependence on the other spatial coordinates is found in the* $m \times m$ *blocks of* (2.36).

The time stepping scheme for the ROM snapshots is obtained from (2.23) and (2.32) and the definition (2.36),

$$\boldsymbol{u}^{\rm ROM}_{j+1} = 2\mathcal{P}^{\rm ROM}\boldsymbol{u}^{\rm ROM}_{j} - \boldsymbol{u}^{\rm ROM}_{|j-1|}, \qquad j \geq 0. \tag{2.38}$$

It is controlled by the ROM propagator $\mathcal{P}^{\rm ROM}$, the symmetric $nm \times nm$ matrix defined as the Galerkin projection of the propagator operator (2.15),

$$\mathcal{P}^{\rm ROM} = \int_\Omega d\boldsymbol{x}\, \boldsymbol{V}^T(\boldsymbol{x})\mathcal{P}\boldsymbol{V}(\boldsymbol{x}). \tag{2.39}$$

This ROM propagator is data driven thanks to (2.21) and definition (2.24),

$$\mathcal{P}^{\rm ROM} = \boldsymbol{R}^{-T}\int_\Omega d\boldsymbol{x}\, \boldsymbol{U}^T(\boldsymbol{x})\mathcal{P}\boldsymbol{U}(\boldsymbol{x})\boldsymbol{R}^{-1} = \boldsymbol{R}^{-T}\boldsymbol{S}\boldsymbol{R}^{-1}. \tag{2.40}$$

**2.4.2. The ROM of the Wave Operator.** The ROM derived from the Galerkin approximation (2.25) describes the evolution of the $nm \times m$ valued ROM wave

$$\widetilde{\boldsymbol{u}}^{\rm ROM}(t) = \int_\Omega d\boldsymbol{x}\, \boldsymbol{V}^T(\boldsymbol{x})\widetilde{\boldsymbol{u}}^{\rm Gal}(t,\boldsymbol{x}) = \int_\Omega d\boldsymbol{x}\, \boldsymbol{V}^T(\boldsymbol{x})\boldsymbol{U}(\boldsymbol{x})\widetilde{\boldsymbol{g}}(t) = \boldsymbol{R}\widetilde{\boldsymbol{g}}(t), \tag{2.41}$$

where again we used (2.21). This wave satisfies the initial conditions

$$\widetilde{\boldsymbol{u}}^{\rm ROM}(0) = \boldsymbol{R}\boldsymbol{e}_0, \qquad \frac{d}{dt}\widetilde{\boldsymbol{u}}^{\rm ROM}(0) = \boldsymbol{0}, \tag{2.42}$$

thanks to (2.33), and it evolves according to the system of ordinary differential equations (ODEs)

$$\frac{d^2}{dt^2}\widetilde{\boldsymbol{u}}^{\rm ROM}(t) + \mathcal{A}^{\rm ROM}\widetilde{\boldsymbol{u}}^{\rm ROM}(t) = \boldsymbol{0}, \qquad t \geq 0. \tag{2.43}$$

The wave operator $\partial_t^2 + \mathcal{A}$ is now replaced by the operator $\frac{d^2}{dt^2} + \mathcal{A}^{\rm ROM}$, where

$$\mathcal{A}^{\rm ROM} = \int_\Omega d\boldsymbol{x}\, \boldsymbol{V}^T(\boldsymbol{x})\mathcal{A}\boldsymbol{V}(\boldsymbol{x}) \tag{2.44}$$

is the Galerkin projection of $\mathcal{A}$, a symmetric $nm \times nm$ matrix. Again, this can be computed from the data thanks to the Gram–Schmidt formula (2.21),

$$\mathcal{A}^{\rm ROM} = \boldsymbol{R}^{-T}\int_\Omega d\boldsymbol{x}\, \boldsymbol{U}^T(\boldsymbol{x})\mathcal{A}\boldsymbol{U}(\boldsymbol{x})\boldsymbol{R}^{-1} = \boldsymbol{R}^{-T}\widetilde{\boldsymbol{S}}\boldsymbol{R}^{-1}. \tag{2.45}$$

Here we used definition (2.28) of $\widetilde{\boldsymbol{S}}$, which can be obtained from the measurements as stated in Theorem 2.

**2.5. Comparison of the ROMs.** How do our ROMs compare with the time domain reduced basis ROMs found in the computational science literature [9, 48, 55], which also use snapshots to define the projection space?

The philosophy behind the reduced basis ROMs stems from principal component analysis in multivariate statistics [51] and the Karhunen–Loève decomposition in stochastic processes modeling [52, 57]. They explore a dynamical system (the wave equation for us) from knowledge of snapshots of the solution. These snapshots are usually discretized in space and the idea is to extract from them a set of uncorrelated vectors, the so-called proper orthogonal decomposition (POD) modes. This can be done via singular value decomposition and the reduced basis is given by the modes corresponding to the significant singular values.

The POD reduced basis ROMs are not useful for waveform inversion, because they require more data than what we can measure at the array. We are also not interested in compressing information. We want to learn how the waves propagate, using the two array data driven ROMs, and then figure out how to estimate the wave speed $c(\boldsymbol{x})$ from them. For the latter task, the algebraic structure of the ROM is very important. It is easier to compute a ROM that approximates the forward map. In particular, in our Galerkin approximations we could have used any basis of $\mathscr{U}$ and we would have obtained a good ROM for approximating this map. But for the inverse problem it is important to use the basis $\boldsymbol{V}(\boldsymbol{x})$, which gives the causal algebraic structure of the ROMs. It is not difficult to see from Theorems 1 and 2 and (2.20) that if we restrict the data to the time instants $j = 0, \ldots, 2J-1$, with $J < n$, then the ROMs will be sensitive to the parts of the medium reached by the wave field up to time $J\tau$. Thus, we can use the ROMs to estimate $c(\boldsymbol{x})$ in a "layer peeling" fashion, first near the array and then deeper inside the medium, by increasing $J$ gradually. This helps the inversion significantly.

Can we say more about the algebraic structures of the ROMs? We can deduce from the ROM time stepping scheme (2.38) evaluated at $j = 0, \ldots, n-1$ and from (2.37) that the ROM propagator $\mathcal{P}^{\text{ROM}}$ is a block tridiagonal matrix. A proof of this fact is found in [18, Appendix C]. The second ROM matrix $\mathcal{A}^{\text{ROM}}$ does not have the same sparse structure, although its entries decay away from the main diagonal, as proved in [20, Appendix D].

The ROM propagator described in section 2.4.1 has surprisingly good approximation properties, meaning that even though it is defined via projection on the space spanned by the first $n$ vector snapshots, it fits the data $\boldsymbol{D}_j$ for $j$ up to $2n-1$. This is proved in [18, Appendix B]. We give here a reformulation of this result, in a slightly weaker form, that is easier to explain and is used in the next section.

THEOREM 3. *The propagator ROM snapshots satisfy, for $j = 0, \ldots, n-1$,*

$$\boldsymbol{D}_j = \int_\Omega d\boldsymbol{x}\, \boldsymbol{u}_0^T(\boldsymbol{x})\boldsymbol{u}_j(\boldsymbol{x}) = (\boldsymbol{u}_0^{ROM})^T \boldsymbol{u}_j^{ROM}, \tag{2.46}$$

$$\boldsymbol{D}_{j+n-1} = \int_\Omega d\boldsymbol{x}\, [2\boldsymbol{u}_{n-1}(\boldsymbol{x}) - \boldsymbol{u}_0(\boldsymbol{x})]^T \boldsymbol{u}_j(\boldsymbol{x}) = [2\boldsymbol{u}_{n-1}^{ROM} - \boldsymbol{u}_0^{ROM}]^T \boldsymbol{u}_j^{ROM}. \tag{2.47}$$

*Proof.* The first equality in (2.46) comes from (2.16). The second equality is because by the definition of $\boldsymbol{U}(\boldsymbol{x})$, the Gram–Schmidt equation (2.21), and the expression (2.37) of the first $n$ ROM snapshots, we get

$$\boldsymbol{u}_j(\boldsymbol{x}) = \boldsymbol{U}(\boldsymbol{x})\boldsymbol{e}_j = \boldsymbol{V}(\boldsymbol{x})\boldsymbol{R}\boldsymbol{e}_j = \boldsymbol{V}(\boldsymbol{x})\boldsymbol{u}_j^{\text{ROM}}, \qquad \boldsymbol{x} \in \Omega, \quad j = 0, \ldots, n-1, \tag{2.48}$$

and therefore

$$\boldsymbol{D}_j = \int_\Omega d\boldsymbol{x} \big[\boldsymbol{V}(\boldsymbol{x})\boldsymbol{u}_0^{\rm ROM}\big]^T \boldsymbol{V}(\boldsymbol{x})\boldsymbol{u}_j^{\rm ROM} \overset{(2.19)}{=} (\boldsymbol{u}_0^{\rm ROM})^T \boldsymbol{u}_j^{\rm ROM}. \tag{2.49}$$

To prove (2.47), we recall the calculation of the mass matrix given in Theorem 1. Setting $i = n-1$ and $j = 0, \ldots, n-1$ in (2.30), we get

$$\boldsymbol{D}_{j+n-1} = 2\int_\Omega d\boldsymbol{x}\, \boldsymbol{u}_{n-1}^T(\boldsymbol{x})\boldsymbol{u}_j(\boldsymbol{x}) - \boldsymbol{D}_{n-1-j}, \tag{2.50}$$

and the result follows from (2.48) and (2.46). ∎

The wave operator ROM described in section 2.4.2 does not fit the data exactly, it only approximates it. This is because the Galerkin wave approximation (2.25) from which it is derived is exact only at $t = 0$, as stated in (2.35), but not at $t = j\tau$ for $1 \le j \le n-1$. To get an exact fit we would have to include the snapshots of the second time derivative of the wave field in the definition of the approximation space. Nevertheless, we will see in the next section that $\mathcal{A}^{\rm ROM}$ is useful for estimating $c(\boldsymbol{x})$, in spite of the inexact data fit.

**2.6. Regularization of the ROM Computation.** The ideal case of noiseless data and linearly independent snapshots that define the approximation space in (2.17) guarantees a positive definite mass matrix $\boldsymbol{M}$ whose square root $\boldsymbol{R}$ can be inverted. In the presence of noise and/or too small time steps $\tau$ and sensor distance separation, the mass matrix $\boldsymbol{M}$ will likely be ill-conditioned, singular, or indefinite. Therefore, regularization is needed to construct the ROMs.

Our approach to regularization is based on spectral projection: Let $\{\lambda_j\}_{j=1}^{nm}$ be the eigenvalues of $\boldsymbol{M}$, in decreasing order, and $\{\boldsymbol{y}_j\}_{j=1}^{nm}$ the corresponding eigenvectors. Let $\epsilon$ be a positive threshold and $r$ be the smallest natural number such that $\lambda_j < \epsilon$ for $rm < j \le nm$. Define the projected mass matrix

$$\boldsymbol{\Lambda}^\epsilon = (\boldsymbol{Y}^\epsilon)^T \boldsymbol{M}\boldsymbol{Y}^\epsilon \in \mathbb{R}^{rm\times rm}, \qquad \boldsymbol{Y}^\epsilon = (\boldsymbol{y}_1, \ldots, \boldsymbol{y}_{rm}) \in \mathbb{R}^{nm\times rm}. \tag{2.51}$$

This matrix is obviously diagonal. The threshold $\epsilon$ should be small, while ensuring a reasonable condition number $\lambda_1/\epsilon$ of $\boldsymbol{\Lambda}^\epsilon$.

Note that $\boldsymbol{\Lambda}^\epsilon$ cannot be our regularized mass matrix, because it does not have the correct block Hankel+Toeplitz structure, which captures the causal wave propagation. To determine the orthogonal transformation that restores this structure, we recall that the ROM propagator must be block tridiagonal. Thus, instead of (2.40), we compute

$$\boldsymbol{\Pi}^\epsilon = (\boldsymbol{\Lambda}^\epsilon)^{-1/2}(\boldsymbol{Y}^\epsilon)^T \boldsymbol{S}\boldsymbol{Y}^\epsilon(\boldsymbol{\Lambda}^\epsilon)^{-1/2} \in \mathbb{R}^{rm\times rm} \tag{2.52}$$

and then use the block Lanczos algorithm [46] to generate the orthogonal matrix $\boldsymbol{Q}^\epsilon \in \mathbb{R}^{rm\times rm}$ that gives the block tridiagonal regularized ROM propagator matrix $\mathcal{P}^{\epsilon,{\rm ROM}} = (\boldsymbol{Q}^\epsilon)^T\boldsymbol{\Pi}^\epsilon\boldsymbol{Q}^\epsilon \in \mathbb{R}^{rm\times rm}$. The regularized mass matrix and its square root are then defined by

$$\boldsymbol{M}^\epsilon = (\boldsymbol{Q}^\epsilon)^T\boldsymbol{\Lambda}^\epsilon\boldsymbol{Q}^\epsilon = (\boldsymbol{R}^\epsilon)^T\boldsymbol{R}^\epsilon \in \mathbb{R}^{rm\times rm}. \tag{2.53}$$

The regularized wave operator ROM follows similarly [20, Appendix E].

**3. Waveform Inversion.** We give two ideas for estimating $c(\boldsymbol{x})$ from our ROMs. The first, described in section 3.2, uses an estimate of the wave field at points inside the medium. This estimate is based on the ROM snapshots of the propagator ROM and is given in section 3.1. The second idea, described in section 3.3, formulates the inversion as a minimization of the wave operator ROM misfit. We summarize the two approaches in section 3.4 and compare them briefly. A more detailed comparison can be found in the numerical simulations in section 3.5.

**3.1. The Estimated Internal Wave.** The chain of mappings from the wave speed $c(\boldsymbol{x})$ to the propagator ROM is

$$c(\boldsymbol{x}) \mapsto \big\{\boldsymbol{D}_j,\ j = 0, \ldots, 2n-1\big\} \mapsto \big\{\mathcal{P}^{\text{ROM}},\ \boldsymbol{u}_j^{\text{ROM}},\ j \geq 0\big\}. \tag{3.1}$$

Both maps in this chain are nonlinear, although we have explained that the second map, from the data to the ROM, can be computed with linear algebra tools. The nonlinear steps in the ROM computation are the Cholesky factorization of the mass matrix $\boldsymbol{M}$, which depends linearly on the data, and the inverse of its Cholesky square root $\boldsymbol{R}$. Inverting the chain of mappings (3.1) to estimate $c(\boldsymbol{x})$ seems as hard as inverting the first map, which is what data fitting does, so how can we use the ROM?

We describe here and in the next section an approach that is inspired by "hybrid inverse problems" like photo-acoustic tomography, transient elastography, etc. In these multiphysics imaging modalities, the propagation of a primary wave inside the inaccessible domain, a.k.a. the "internal wave," is monitored with high time and space resolution by a second type of wave. The point is that knowledge of the internal wave considerably simplifies the inversion for the unknown coefficients of the governing PDE [59, 5, 3]. Hybrid approaches are mostly limited to medical applications, because they involve delicate and accurate user-controlled apparatus for transmitting several types of waves and measuring all around the body of interest. We propose to use the ROM for estimating the internal waves, without any additional measurements.

The main idea for the estimation comes from (2.48), which relates the data driven ROM snapshots $\boldsymbol{u}_j^{\text{ROM}}$, which are matrices, to the true vector snapshots $\boldsymbol{u}_j(\boldsymbol{x})$ defined by (2.13), which are $\boldsymbol{x}$ dependent fields, for $\boldsymbol{x} \in \Omega$. This relationship involves the orthonormal basis $\boldsymbol{V}(\boldsymbol{x})$, which cannot be computed, but has properties that are useful for inversion. So far, these properties are only partially understood: It is proved in [19, Appendix A] using explicit calculations in a layered medium and in a waveguide that $\boldsymbol{V}(\boldsymbol{x})$ is insensitive to the reflectivity (rough part of $c(\boldsymbol{x})$) but depends on the kinematics (smooth part of $c(\boldsymbol{x})$). Extensive numerical simulations carried out in [16, 33, 19, 20] suggest that this property extends to more general settings as well.

In many, but not all applications, the kinematics is only mildly perturbed, so these results originally motivated our definition of the estimated internal wave snapshots,

$$\boldsymbol{u}_j^{\text{est}}(\boldsymbol{x}; w) = \boldsymbol{V}(\boldsymbol{x}; w)\boldsymbol{u}_j^{\text{ROM}} = \boldsymbol{V}(\boldsymbol{x}; w)\boldsymbol{R}\boldsymbol{e}_j, \quad j = 0, \ldots, n-1, \quad \boldsymbol{x} \in \Omega, \tag{3.2}$$

where $\boldsymbol{V}(\boldsymbol{x}; w)$ is the orthonormal basis computed for the search wave speed $w(\boldsymbol{x})$. Why is this better than the linearization of the forward mapping used by any iterative inversion algorithm? That would approximate the internal wave snapshots by

$$\boldsymbol{u}_j(\boldsymbol{x}; w) = \cos\big[j\tau\sqrt{\mathcal{A}(w)}\big]\boldsymbol{u}_0(\boldsymbol{x}) = \boldsymbol{V}(\boldsymbol{x}; w)\boldsymbol{R}(w)\boldsymbol{e}_j, \quad j = 0, \ldots, n-1, \quad \boldsymbol{x} \in \Omega, \tag{3.3}$$

where $\mathcal{A}(w) = -w(x)\Delta\big[w(x)\cdot\big]$ and $\boldsymbol{R}(w)$ is the Cholesky square root of the mass matrix computed from the simulated data at wave speed $w(\boldsymbol{x})$. The advantage of (3.2) over (3.3) is that it is consistent with the measurements, as stated next.

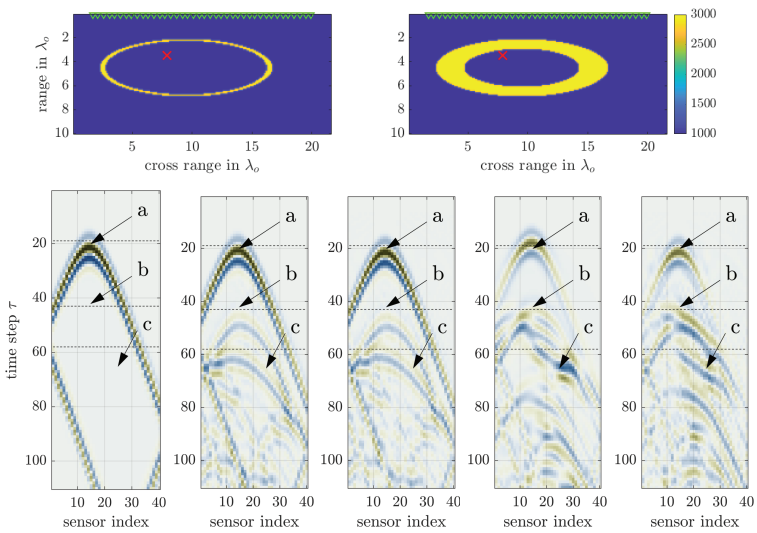


**Fig. 3.1** *Illustration of the internal waves at $\boldsymbol{x}$ indicated with red $\times$ in two media containing a ring-shaped inclusion (top plots). The active array is linear and placed at the top of the plots, with sensors indicated by green triangles. The wave speed is shown in the colorbar in units of m/s. The axes are cross-range (measured along the array) and range (measured orthogonal to the array) in units of the central wavelength. The bottom plots show the internal waves as functions of the sensor index s (abscissa) and time in units of $\tau$ (ordinate). From left to right: $u^{(s)}(j\tau, \boldsymbol{x}; w = \bar{c})$ calculated with the constant wave speed $\bar{c} = 1$km/s; the true wave $u^{(s)}(j\tau, \boldsymbol{x})$ in the first medium; the estimated $u^{(s),\text{est}}(j\tau, \boldsymbol{x}; w = \bar{c})$ in the first medium; the true wave $u^{(s)}(j\tau, \boldsymbol{x})$ in the second medium; and the estimated $u^{(s),\text{est}}(j\tau, \boldsymbol{x}; w = \bar{c})$ in the second medium.*

COROLLARY 1. *The estimated internal wave snapshots* (3.2) *fit the data*

$$\boldsymbol{D}_j = \int_\Omega d\boldsymbol{x}\, \boldsymbol{u}_0(\boldsymbol{x})^T \boldsymbol{u}_j(\boldsymbol{x}) = \int_\Omega d\boldsymbol{x}\, \boldsymbol{u}_0^{\text{est}}(\boldsymbol{x})^T \boldsymbol{u}_j^{\text{est}}(\boldsymbol{x}),$$

$$\boldsymbol{D}_{j+n-1} = \int_\Omega d\boldsymbol{x}\, [2\boldsymbol{u}_{n-1}(\boldsymbol{x}) - \boldsymbol{u}_0(\boldsymbol{x})]^T \boldsymbol{u}_j(\boldsymbol{x}) = \int_\Omega d\boldsymbol{x}\, [2\boldsymbol{u}_{n-1}^{\text{est}}(\boldsymbol{x}) - \boldsymbol{u}_0^{\text{est}}(\boldsymbol{x})]^T \boldsymbol{u}_j^{\text{est}}(\boldsymbol{x})$$

*for $j = 0, \ldots, n-1$, whereas $\boldsymbol{u}_j(\boldsymbol{x}; w)$ defined in* (3.3) *do not.*

*Proof.* The proof follows easily from that of Theorem 3, because (2.49) holds if we replace $\boldsymbol{V}(\boldsymbol{x})$ by any orthonormal basis, like $\boldsymbol{V}(\boldsymbol{x}; w)$. The data fit is ensured by the ROM snapshots $\boldsymbol{u}_j^{\text{ROM}} = \boldsymbol{R}\boldsymbol{e}_j$ for $j = 0, \ldots, n-1$, irrespective of the basis. Obviously, if we replace $\boldsymbol{R}$ by $\boldsymbol{R}(w)$, we no longer fit the data, so the snapshots (3.3) are not consistent with the measurements. ∎

To illustrate this result, we display in Figure 3.1 the internal waves at a point $\boldsymbol{x}$ inside two media with a fast ring-shaped inclusion with wave speed 3km/s, in a background of wave speed $\bar{c} = 1$km/s. The difference between the media is the thickness of the ring: In the first medium the ring is thin, so the kinematics is only slightly perturbed. In the second medium the ring is thick, so the perturbation of the kinematics is more significant. The true internal waves are in the second and fourth bottom plots. They display three types of arrivals: (1) The direct arrival (the hyperbola denoted by $a$) of the wave that travels from the array to $\boldsymbol{x}$, through the inclusion. (2) The echoes that have bounced between the inclusion and the top

boundary, like those denoted by $b$ and $c$ in the plot. (3) The echoes from the side boundaries of the domain $\Omega$. The bottom left plot shows the wave (3.3) calculated with $w \equiv \bar{c}$. It is quite different from the true waves, as it contains only the direct arrival and the echoes from the side boundaries. The third and fifth bottom plots show our estimate (3.2) of the internal wave in the two media for the same $w \equiv \bar{c}$. They are quite similar to the true waves and contain all the arrivals. This is because the information about these arrivals is in $\boldsymbol{R}$, which is responsible for the data fit stated in Corollary 1. The purpose of $\boldsymbol{V}(\boldsymbol{x}; w)$ in (3.2) is to map these arrivals from the algebraic (ROM) space to the physical space. Because we do not use the right kinematics and this significantly affects $\boldsymbol{V}(\boldsymbol{x}; w = \bar{c})$ in the case of the thick ring, we can see that the arrivals are delayed in the bottom fifth plot compared to the true internal wave in the bottom fourth plot.

**3.2. Inversion with the Estimated Internal Wave.** It is well known that the forward map, which relates $c(\boldsymbol{x})$ to the wave measured at the array, is given by the Lippmann–Schwinger integral equation. Due to the transformations described in section 2.1, this equation has the following form derived in [21, Proposition 4.1]:

$$D_{r,s}(t) - D_{r,s}(t; w) = \int_0^t dt' \int_\Omega d\boldsymbol{x}\, \frac{[c^2(\boldsymbol{x}) - w^2(\boldsymbol{x})]}{c(\boldsymbol{x}) w(\boldsymbol{x})} u^{(s)}(t', \boldsymbol{x}) \partial_{t'} u^{(r)}(t', \boldsymbol{x}; w), \tag{3.4}$$

where we recall that in our notation convention we add $w$ to the arguments of the fields computed with the search speed $w(\boldsymbol{x})$ and suppress $c(\boldsymbol{x})$ in the arguments of the fields corresponding to the true speed.

Equation (3.4) shows that the mapping $c(\boldsymbol{x}) \mapsto \boldsymbol{D}(t)$ is nonlinear not only because of the way $c(\boldsymbol{x})$ enters the first factor of the integrand, but also because the internal wave $u^{(s)}(t', \boldsymbol{x})$ depends on $c(\boldsymbol{x})$ in a very complicated way. The first inversion approach introduced in [21] is to replace this wave by the estimate (3.2). The iterative optimization based on the resulting mapping works better than that of FWI, as long as the kinematics is not too perturbed [21, section 5]. Otherwise, the iteration can get stuck, like that of FWI.

Since the improvement brought about by the estimated internal wave in data fitting is marginal, is there a better way to use it? The new idea that we now describe takes the following point of view: Corollary 1 states that the estimated internal wave is consistent with the measurements by construction, so why should we seek to fit the data at all? The estimate (3.2) is not guaranteed to be an approximate solution of the wave equation. If that were the case, then $w(\boldsymbol{x})$ would be close to the solution $c(\boldsymbol{x})$ of the inverse problem.[2]

How can we enforce $\boldsymbol{u}_j^{\text{est}}(\boldsymbol{x}; w)$ to be close to the solution $\cos\big[j\tau\sqrt{\mathcal{A}(w)}\,\big]\boldsymbol{u}_0(\boldsymbol{x})$ of the wave equation for $j = 0, \dots, n-1$? First, we note that $\boldsymbol{u}_0(\boldsymbol{x})$ is known because it depends on the medium near the array, where the wave speed equals the given constant $\bar{c}$. Second, we obtain from definitions (3.2) and (3.3) that the quadratic misfit between the estimated internal wave $\boldsymbol{u}_j^{\text{est}}(\boldsymbol{x}; w)$ and the solution $\cos\big[j\tau\sqrt{\mathcal{A}(w)}\,\big]\boldsymbol{u}_0(\boldsymbol{x})$ is

$$\begin{aligned}\int_\Omega d\boldsymbol{x} \sum_{j=0}^{n-1} \big\|\boldsymbol{u}_j^{\text{est}}(\boldsymbol{x}; w) - \cos\big[j\tau\sqrt{\mathcal{A}(w)}\,\big]\boldsymbol{u}_0(\boldsymbol{x})\big\|_{\text{F}}^2 &= \int_\Omega d\boldsymbol{x} \big\|\boldsymbol{V}(\boldsymbol{x}, w)\big[\boldsymbol{R} - \boldsymbol{R}(w)\big]\big\|_{\text{F}}^2 \\ &= \|\boldsymbol{R} - \boldsymbol{R}(w)\|_{\text{F}}^2,\end{aligned} \tag{3.5}$$

[2]This is assuming that $c(\boldsymbol{x})$ can be determined uniquely for the given measurement setup and the inversion is stable due to proper regularization and parametrization of the search speed.

because $\int_\Omega d\boldsymbol{x}\boldsymbol{V}^T(\boldsymbol{x},w)\boldsymbol{V}(\boldsymbol{x},w) = \boldsymbol{I}_{nm}$ for any $w$. Thus, we can just minimize the misfit of the Cholesky square roots of the data driven mass matrices.

We consider a modification of this objective function, given by

$$\mathcal{O}(w) = \|\boldsymbol{R}(w)^{-1}\boldsymbol{R} - \boldsymbol{I}_{nm}\|_{\rm F}^2. \tag{3.6}$$

This is motivated by the following observation: Variations in the medium that are closer to the array give much stronger echoes than those that are further away. The information about the latter is encoded in the smaller entries of $\boldsymbol{M}$ and, consequently, the smaller singular values of $\boldsymbol{R}$. To balance these contributions, we emphasize the weaker events by taking the inverse of $\boldsymbol{R}(w)$ in (3.6). Here we ignore that $\boldsymbol{R}(w)$ may be ill-conditioned, but this can be addressed by regularization as explained in section 2.6 and in [20, Appendix E].

**3.3. Inversion with the ROM Wave Operator.** The second objective function for ROM based waveform inversion was introduced recently in [20]. It measures the wave operator ROM misfit

$$\widetilde{\mathcal{O}}(w) = \|\mathcal{A}^{\rm ROM} - \mathcal{A}^{\rm ROM}(w)\|_{\rm F}^2, \tag{3.7}$$

where $\mathcal{A}^{\rm ROM}$ is obtained from the data by (2.45) using the matrices $\boldsymbol{R}$ and $\widetilde{\boldsymbol{S}}$ built in Theorems 1–2. The matrix $\mathcal{A}^{\rm ROM}(w)$ is obtained from the synthetic data simulated with the wave speed $w(\boldsymbol{x})$.

Note that in (3.7) we do not penalize the data misfit and, as explained in section 2.5, the ROM wave $\widetilde{\boldsymbol{u}}^{\rm ROM}(t)$ does not reproduce the measurements exactly. Thus, unlike the approach described in the previous section, based on the estimated internal wave, we cannot expect an automatic data fit here. Nevertheless, the data are fit approximately, because the ROM comes from a Galerkin approximation of the wave equation. Our motivation for using the objective function (3.7) is threefold:

1. The operator $\mathcal{A}$ depends in a simple way on the unknown $c(\boldsymbol{x})$, unlike the propagator $\mathcal{P}$. Indeed, fitting $\boldsymbol{\mathcal{P}}^{\rm ROM}$ is not a good idea, as illustrated in section 3.5.
2. The projection basis $\boldsymbol{V}(\boldsymbol{x})$ depends on $c(\boldsymbol{x})$, which makes the analysis of (3.7) very complicated. However, the existing theoretical results and numerous numerical simulations suggest that the change of this basis with $c(\boldsymbol{x})$ is slower than that of $\mathcal{A}$. In other words, we expect that $\mathcal{A}^{\rm ROM}$ is approximately quadratic in the wave speed $c(\boldsymbol{x})$. This is not the case for the data matrices used in the FWI objective function.
3. Numerical evidence [20, 16] suggests that the $m$ components of the $\boldsymbol{v}_j(\boldsymbol{x})$ block of $\boldsymbol{V}(\boldsymbol{x})$ are localized around the maximum depth reached by the wave field at time $j\tau$. Thus, definition (2.44) suggests that the entries in $\mathcal{A}^{\rm ROM}$ depend mostly on local averages of $c(\boldsymbol{x})$, as is usual in standard Galerkin approximation schemes.

**3.4. The Inversion Algorithms. Pros and Cons.** Here we give the pseudo-algorithms that summarize the steps in our two inversion approaches, and then we compare them. Both algorithms require a parametrization of the search velocity space,

$$w(\boldsymbol{x}) = \bar{c} + \sum_{j=1}^N \eta_j \phi_j(\boldsymbol{x}), \qquad \boldsymbol{\eta} = (\eta_1, \ldots, \eta_N) \in \mathbb{R}^N, \tag{3.8}$$

using some user-defined basis functions $\{\phi_j(\boldsymbol{x})\}_{j=1}^N$ for $\boldsymbol{x} \in \Omega$.

**Algorithm 3.1** Inversion with the internal wave.

**Input:** Data matrices $\{\boldsymbol{D}_j\}_{j=0}^{2n-1}$ calculated from the measurements as in Lemma 1 and the reference speed $\bar{c}$.

1. Compute $\boldsymbol{M}$ with block entries given in (2.31). If $\boldsymbol{M}$ is indefinite or singular, use regularization as described in section 2.6.
2. Compute the block Cholesky square root $\boldsymbol{R}$ of $\boldsymbol{M}$ or its regularized version.
3. Starting with the initial vector $\boldsymbol{\eta} = \boldsymbol{\eta}^{(0)} = \boldsymbol{0}$ in (3.8), proceed as follows:
   - For update index $j \geq 1$, calculate $w(\boldsymbol{x})$ as in (3.8), with $\boldsymbol{\eta} = \boldsymbol{\eta}^{(j-1)}$.
   - Calculate $\boldsymbol{R}(w)$ following the same procedure for calculating $\boldsymbol{R}$.
   - Compute $\boldsymbol{\eta}^{(j)}$ as a Gauss–Newton update for minimizing the objective function (3.6) with the user's choice of the regularization penalty on $\boldsymbol{\eta}$.
   - Go to the next iteration or stop when the convergence criterion is met.

**Output:** The estimate of the wave speed given by (3.8) with $\boldsymbol{\eta}$ calculated at step 3.

**Algorithm 3.2** Inversion with the wave operator ROM.

**Input:** Data matrices $\{\boldsymbol{D}_j\}_{j=0}^{2n-1}$ calculated from the measurements as in Lemma 1 and the reference speed $\bar{c}$.

1. Compute $\{\ddot{\boldsymbol{D}}_j\}_{j=0}^{2n-2}$ using, for example, the Fourier transform.
2. Compute $\boldsymbol{M}$ with the block entries given in (2.31) and $\widetilde{\boldsymbol{S}}$ with the block entries (2.34). If needed, regularized matrices can be computed (see [20, Appendix E]).
3. Compute the block Cholesky square root of $\boldsymbol{M}$ or its regularized version and the wave operator ROM $\mathcal{A}^{\text{ROM}}$ using the right-hand side in (2.45).
4. Starting with the initial vector $\boldsymbol{\eta} = \boldsymbol{\eta}^{(0)} = \boldsymbol{0}$ in (3.8), proceed as follows:
   - For update index $j \geq 1$, calculate $w(\boldsymbol{x})$ as in (3.8), with $\boldsymbol{\eta} = \boldsymbol{\eta}^{(j-1)}$.
   - Calculate $\mathcal{A}^{\text{ROM}}(w)$ following the same procedure for calculating $\mathcal{A}^{\text{ROM}}$.
   - Compute $\boldsymbol{\eta}^{(j)}$ as a Gauss–Newton update for minimizing the objective function (3.7) with the user's choice of the regularization penalty on $\boldsymbol{\eta}$.
   - Go to the next iteration or stop when the convergence criterion is met.

**Output:** The estimate of the wave speed given by (3.8) with $\boldsymbol{\eta}$ calculated at step 4.

When we compare the two approaches, we note that Algorithm 3.1 is easier to use, as it involves only the mass matrix and its block Cholesky square root. Moreover, if the objective function (3.6) is small, then the data are fit implicitly by Corollary 1. Algorithm 3.2 is slightly more expensive computationally, because it requires the computation of the second derivatives of the data matrices and the wave operator ROM. Moreover, the data are not fit as well as in the first approach. Nevertheless, the numerical results show that both approaches give comparable estimates of the wave speed. In fact, in a few numerical experiments (see Figure 3.4), we see a slightly better result with Algorithm 3.2.

**3.5. Numerical Results and Comparison of the Inversion Approaches.** We refer to Appendix A for the details of our numerical simulations. Here we compare the inversion approaches by visualizing the objective functions in a two-dimensional search space (section 3.5.1) and by showing the inversion results for three well-known

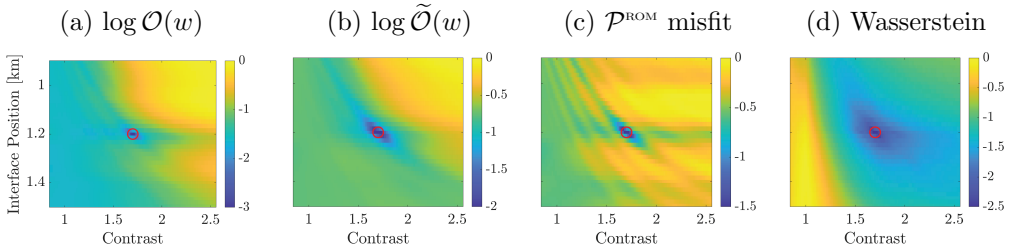


**Fig. 3.2** *Display of the log of the objective functions for the setup in Figure* 1.1. *The axes are the same as in the right plot there. The true model is indicated by* ◯.

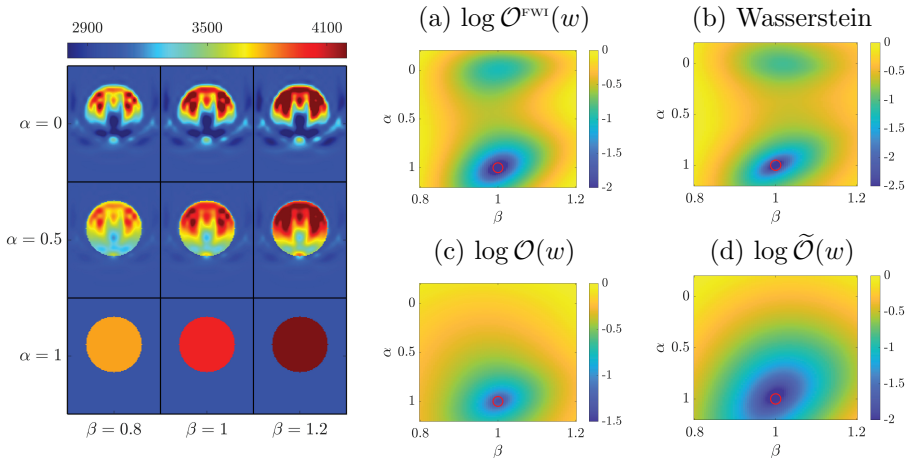


**Fig. 3.3** *Left plot: Illustration of the search speed* (3.9) *for* 9 *choices of* $\alpha$ *and* $\beta$. *Right plots: Log of objective functions parametrized by* $\beta$ *(abscissa) and* $\alpha$ *(ordinate). The true model is indicated by* ◯.

challenging media (section 3.5.2). We discuss in section 3.5.3 the computational cost and compare it to that of FWI.

**3.5.1. Visualization of the Objective Functions.** One way to compare the various inversion approaches is to visualize their objective functions using a two-dimensional search space. We begin in Figure 3.2 with the objective functions for the setup in Figure 1.1, where the multiple minima of the FWI objective function were clearly visible. We note that both ROM objective functions (3.6) (plot (a)) and (3.7) (plot (b)) have a single minimum at the correct location. In plot (c) we display the log of the propagator ROM misfit $\|\mathcal{P}^{\rm ROM} - \mathcal{P}^{\rm ROM}(w)\|_{\rm F}^2$ to show that it is not a good choice for the inversion. This is not surprising, because the sought-after $c(\boldsymbol{x})$ appears in a very complicated way in the expression of the propagator operator defined in (2.15). The plot (d) shows that if, instead of quantifying the data misfit in the $L^2([t_{\min}, t_{\max}])$ norm as in FWI, we use the Wasserstein metric, computed as described in [35], we end up with a better objective function, with a single minimum at the correct location.

To show the advantage of using the ROM based objective functions, next we consider a challenging example, coined as the "Camembert" model in the geophysics community [43]. It consists of a piecewise constant $c(\boldsymbol{x})$, modeling a disk-shaped fast inclusion embedded in a homogeneous medium with wave speed $\bar{c} = 3$km/s (left

plot in Figure 3.4). The name is coined because FWI, starting from the initial guess $w(\boldsymbol{x}) = \bar{c}$, can only recover well the top of the inclusion and the estimate $c^{\text{FWI}}(\boldsymbol{x})$ of $c(\boldsymbol{x})$ "melts away" from there, as would Camembert cheese. The details of the inversion are in the next section and Appendix A. Here, we display in Figure 3.3 the objective functions in a two-dimensional search space with wave speed

$$w(\boldsymbol{x};\alpha,\beta) = \bar{c} + \beta\left\{(1-\alpha)\left[c^{\text{FWI}}(\boldsymbol{x}) - \bar{c}\right] + \alpha\left[c(\boldsymbol{x}) - \bar{c}\right]\right\} \tag{3.9}$$

parametrized by $\alpha \in [-0.2, 1.2]$ and $\beta \in [0.8, 1.2]$. Note how $\alpha$ interpolates between the FWI estimate and the true wave speed. The parameter $\beta$ is used to vary the contrast. Figure 3.3 shows that the objective functions based on data fitting (plots (a) and (b)) have two minima. The ROM objective functions (plots (c) and (d)) have a single minimum at the true speed, i.e., $\alpha = 1$ and $\beta = 1$.

**3.5.2. Inversion Results.** We present results for three known challenging media. All are in two dimensions for a linear array of colocated sources and receivers. Carrying out the inversion in three dimensions involves no conceptual change, but, naturally, the computational cost is higher. This is discussed in section 3.5.3 and [20].

The minimization of the objective functions is carried out with the Gauss–Newton method, in an $N$-dimensional search space $\mathcal{W}$ with $w(\boldsymbol{x})$ of the form (3.8), spanned by $N$ Gaussian basis functions $\phi_l(\boldsymbol{x}) = \frac{1}{2\pi\sigma^{\perp}\sigma}\exp\left[-\frac{(x^{\perp}-x_l^{\perp})^2}{2(\sigma^{\perp})^2} - \frac{(x-x_l)^2}{2\sigma^2}\right]$ with peaks at the points $\boldsymbol{x}_l = (x_l^{\perp}, x_l)$ on a uniform grid discretizing the inversion domain $\Omega_{\text{inv}} \subset \Omega$. Here, $x_l^{\perp}$ denotes the cross-range coordinate (along the array) and $x_l$ is the range coordinate, in the direction orthogonal to the array. The standard deviations of the Gaussian functions in these directions are $\sigma^{\perp}$ and $\sigma$.

We do not discuss noise effects on the inversion, but these have been addressed in [20, 21]. Even in the absence of noise, diffraction limits the resolution of the inversion to about half the central wavelength. In our simulations we overparametrize $\mathcal{W}$, so we add the Tikhonov regularization penalty $\mu\|\boldsymbol{\eta}\|_2^2$ to the objective functions, with $\mu$ chosen adaptively during the iteration, as explained in [20, Appendix D].

The inversion is carried out in a layered peeling fashion by time windowing the data, as explained in section 2.5. If we use $N_t$ windows, then each one is of the form $t_{\min} \le t \le t_{q,\max}$, where $t_{q,\max} = t_{\min} + \frac{q}{N_t}[t_{\max} - t_{\min}]$ and $q = 1, \ldots, N_t$. The updates of the wave speed for the $q$th window are computed up to the maximum depth sensed by the waves at $t \le t_{q,\max}$. This depth can be estimated in practice using some conservative upper bound on $c(\boldsymbol{x})$. In our experience, the results are not very sensitive to this depth. The parameters for the results below are in Appendix A.

The first results are for the Camembert model. We show in Figure 3.4 the estimated wave speed after 60 Gauss–Newton iterations, although the FWI approach stagnated after 30 iterations. The initial guess is the constant speed $\bar{c} = 3$km/s. Clearly, both ROM based methods give a good estimate of the fast inclusion, while FWI does not.

The second set of results is for the model displayed in the top left plot of Figure 3.5. It was proposed in [10] as a challenge problem for imaging behind a salt body in the earth (the top fast structure in the figure, with wave speed 4.5km/s). The initial guess is shown in the top right plot. The inversion results displayed in the bottom plots are obtained after 35 Gauss–Newton iterations. They show that the ROM based methods perform similarly and image well. The FWI approach determines the top features of the salt body, but then it gets stuck in a local minimum after 26 iterations.

The third (and last) results are for a realization of a smooth random medium (with Gaussian statistics and Gaussian covariance function), where the wave speed

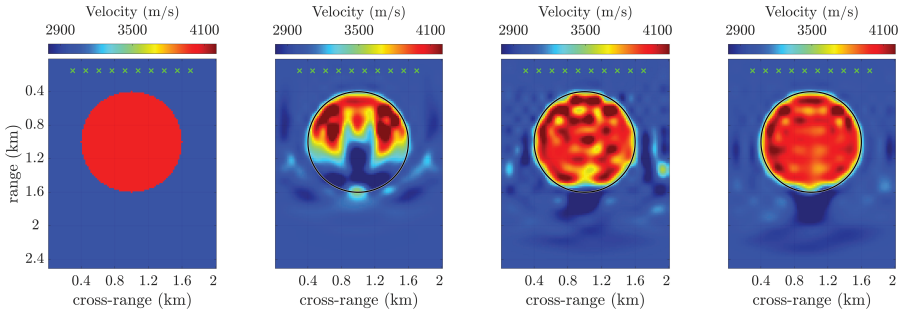


**Fig. 3.4** *Inversion results. From left to right: True velocity $c(\boldsymbol{x})$; velocity estimated by FWI objective* (1.5)*, by ROM objective* (3.6)*, and by ROM objective* (3.7)*. The sources/receivers are shown with green ×.*

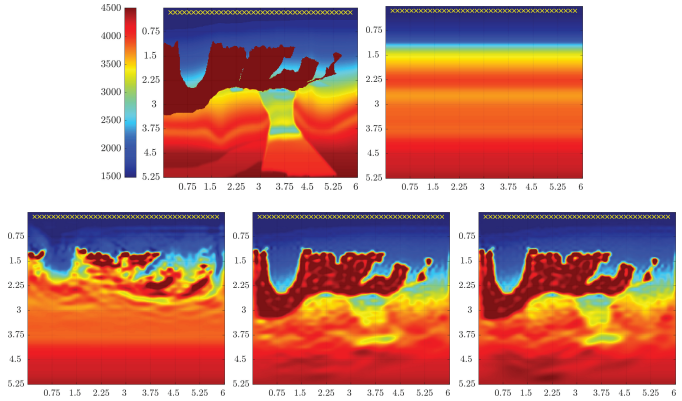

**Fig. 3.5** *Top row, left to right: True $c(\boldsymbol{x})$ and initial guess. Bottom row, left to right: Velocity estimated by FWI objective* (1.5)*, by ROM objective* (3.6)*, and by ROM objective* (3.7)*. Sources/receivers are shown with yellow ×. The plots use the same colorbar.*

fluctuates about the reference value $\bar{c} = 1.5$km/s. The true medium is shown in the left plot and the reconstructed one is in the right plot of Figure 3.6. It is obtained after 135 Gauss–Newton iterations for the operator ROM misfit (3.7) with Tikhonov regularization. The initial guess is the constant speed $\bar{c} = 1.5$km/s. We assess the quality of the reconstruction in two ways: First, we compute the correlation coefficient of the two images in Figure 3.6 in the domain $[0.75\text{km}, 6\text{km}] \times [0.5\text{km}, 5.25\text{km}]$ with the MATLAB command "corr2." A perfect reconstruction would give a correlation coefficient equal to 1. The correlation coefficient for our reconstruction is 0.613. This may seem low, but we should remember that it is impossible to find the true medium due to physical constraints on the resolution limit. The second and better way to compare is to use a time-reversal experiment [37, 38]. A time-reversal experiment consists of two steps. In the first step, waves transmitted by a controlled source and scattered by an unknown, complex medium are recorded by an array of sensors used as receivers. In the second step, the array of sensors used as sources transmits the time-reversed recorded signals. One observes a refocusing of the wave at the original source location due to the time reversibility of the wave equation. Moreover, time-reversal refocusing is sensitive to any relevant change in the medium between the two steps [1, 6]. This means that changes in the medium that affect the wave

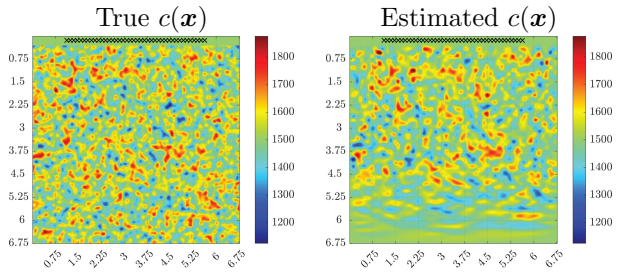


**Fig. 3.6** *Inversion result using the operator ROM. The sources/receivers are shown with black ×. The abscissa and ordinate are the cross-range and range in km and the wave speed values are in the colorbar, in m/s.*

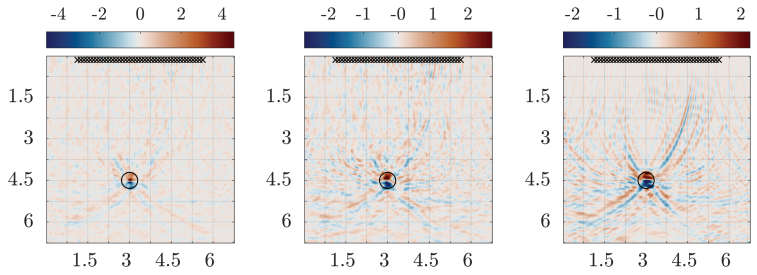

**Fig. 3.7** *Time-reversal focusing in the true medium (left), the estimated medium (middle), and the reference homogeneous medium (right) at a point labeled by a circle. The abscissa and ordinate are the cross-range and range in km.*

scattering process have a strong impact on the refocusing. A time-reversal experiment can be used, therefore, to check whether or not an estimation of a wave speed by an imaging method is correct. Here, we solve the wave equation with a point source at location (3km, 4.5km) in the true medium and register the wave field at the array for $t \in [0, 5.8\text{s}]$. We time reverse these waves and send them back (computationally) into three media: the true one, the estimated one, and the reference (homogeneous) medium. The back-propagated wave refocuses at the original source location in the true medium (left plot in Figure 3.7). The more different the backpropagation medium is from the true one, the worse the refocusing is. Indeed, refocusing is poor in the reference medium (right plot in Figure 3.7), but it is much improved in the estimated medium (middle plot in Figure 3.7). This demonstrates that the estimated wave speed is similar to the one perceived by the waves in the true medium.

**3.5.3. Computational Cost.** Since both our inversion approaches use a Gauss–Newton iteration to minimize the objective functions (3.6) or (3.7), we compare their computational cost to that of the Gauss–Newton method for minimizing the FWI objective function (1.5). The same parametrization (3.8) of the search velocity is assumed for all the approaches.

If the number $m$ of sensors and the number $2n-1$ of time steps is not too large, then the cost of each Gauss–Newton iteration is dominated by the computation of the Jacobian of the objective function. For the FWI objective function, there is an efficient way to compute the Jacobian using the so-called adjoint formula [65, 62]. The analogues of such a formula for the objective functions (3.6) and (3.7) have not been derived, yet. Thus, our calculation of the Jacobian using finite differences is the

bottleneck of the computations. Aside from the Jacobian, the main computational burden of our approaches is due to the block Cholesky factorization of the mass matrix, which involves $O\big((nm)^3\big)$ operations.

If $nm \gg 1$, as happens in three-dimensional simulations, the dominant computational cost is in solving the normal equations for the Gauss–Newton updates. This can be handled using iterative methods, such as conjugate gradient. To manage the extra computational burden of our method, one can compute the objective functions (3.6) and (3.7) from data gathered by subarrays and then sum them in the optimization. This idea has been used successfully for a different problem in [15]. In addition, one can exploit the algebraic structure of the wave operator ROM to define a new objective function that quantifies the misfit of a few block diagonals of $\mathcal{A}^{\text{ROM}}$ [20].

**4. Passive Data Acquisition.** So far, we have assumed knowledge of the array response matrix $\boldsymbol{\mathcal{M}}(t)$, gathered by colocated sources and receivers, which we then transformed to the new data matrix $\boldsymbol{D}(t)$, as stated in Lemma 1. In this section we consider uncontrolled, ambient noise sources that emit stationary random signals and show how the cross-correlations of the generated waves measured at a passive array of receivers can give the matrix $\boldsymbol{D}(t)$ directly. This opens the door to new applications in which the use of controlled active sources is neither possible nor desired.

The fact that the cross-correlations of the signals measured by a passive array can give the same information as an active array is not new [56], and it has been exploited for many problems in imaging and free space communications [40, 41, 42, 39]. The mathematical statement is that the cross-correlations of the signals are related to the symmetrized Green's function of the wave equation. This relationship holds for different situations, in open media with radiation conditions and in bounded cavities. To stay consistent with the rest of the paper, we address here the case of a bounded cavity with homogeneous Dirichlet boundary conditions.

For a well-posed mathematical formulation of the problem with random noise sources, we need to introduce some dissipation. Thus, we consider the solution $p(t,\boldsymbol{x})$ of the damped wave equation $(T_a^{-1}+\partial_t)^2 p - c^2(\boldsymbol{x})\Delta p = s(t,\boldsymbol{x})$ in dimension $d \in \{2,3\}$, where the forcing term $s(t,\boldsymbol{x})$ is a zero-mean, stationary-in-time random process. As in section 2.1, we apply the similarity transformation (2.1) from $p(t,\boldsymbol{x})$ to $P(t,\boldsymbol{x})$, which acts as the identity at the points in the receiver array. This transforms the wave operator to $(T_a^{-1}+\partial_t)^2 + \mathcal{A}$. The source term becomes $S(t,\boldsymbol{x}) = s(t,\boldsymbol{x})\bar{c}/c(\boldsymbol{x})$, and we model its autocorrelation by

$$\langle S(t_1,\boldsymbol{y}_1)S(t_2,\boldsymbol{y}_2)\rangle = F(t_1-t_2)K(\boldsymbol{y}_1)\delta(\boldsymbol{y}_1-\boldsymbol{y}_2), \tag{4.1}$$

where $\langle\cdot\rangle$ denotes a statistical average. In this equation, the function $K(\boldsymbol{y})$ characterizes the spatial support of the noise sources, which is assumed to be contained in $\Omega$. The sources are delta-correlated in space, hence the Dirac delta in (4.1), and the covariance in time depends only on the time offset $t_1 - t_2$ because of stationarity. The function $F(t)$ decays to 0 at infinity, is even, and belongs to $L^1$ (which gives it ergodic properties). The Fourier transform $\widehat{F}(\omega)$ of $F(t)$ is the power spectral density of the noise sources, which is nonnegative by Bochner's theorem.

For any $\boldsymbol{y} \in \Omega$, the Green's function $(t,\boldsymbol{x}) \mapsto G(t,\boldsymbol{x},\boldsymbol{y})$ is the solution of

$$(T_a^{-1}+\partial_t)^2 G + \mathcal{A}G = \delta(t)\delta(\boldsymbol{x}-\boldsymbol{y}), \qquad t \in \mathbb{R}, \quad \boldsymbol{x} \in \Omega, \tag{4.2}$$

with the initial condition $G(t,\boldsymbol{x},\boldsymbol{y}) = 0$ for all $t < 0$ and the boundary condition $G(t,\boldsymbol{x},\boldsymbol{y}) = 0$ for $\boldsymbol{x} \in \partial\Omega$. It can be written explicitly in terms of the eigenvalues

$\{\theta_j\}_{j\geq 1}$ and orthonormal eigenfunctions $\{y_j(\boldsymbol{x})\}_{j\geq 1}$ of $\mathcal{A}$, as follows:

$$G(t,\boldsymbol{x},\boldsymbol{y}) = H(t)\exp(-t/T_a)\sum_{j=1}^{\infty}\theta_j^{-\frac{1}{2}}\sin(\sqrt{\theta_j}t)y_j(\boldsymbol{x})y_j(\boldsymbol{y}), \tag{4.3}$$

where we recall that $H(t)$ is the Heaviside step function.

The empirical cross-correlation of the waves recorded at $\boldsymbol{x}_r$ and $\boldsymbol{x}_{r'}$ is defined by

$$C_T(\tau,\boldsymbol{x}_r,\boldsymbol{x}_{r'}) = \frac{1}{T}\int_0^T dt\, P(t,\boldsymbol{x}_r)P(t+\tau,\boldsymbol{x}_{r'}), \tag{4.4}$$

and the statistical cross-correlation $C^{(1)}(\tau,\boldsymbol{x}_r,\boldsymbol{x}_{r'}) = \big\langle C_T(\tau,\boldsymbol{x}_r,\boldsymbol{x}_{r'})\big\rangle$ is independent of $T$ by stationarity of the noise sources. The statistical stability of (4.4) follows from the ergodicity of the noise sources [42] and $C_T(\tau,\boldsymbol{x}_r,\boldsymbol{x}_{r'}) \overset{T\to+\infty}{\longrightarrow} C^{(1)}(\tau,\boldsymbol{x}_r,\boldsymbol{x}_{r'})$, in probability. The relationship between the statistical cross-correlation and the Green's function can be obtained by using the normal mode expansion (4.3). The next proposition, stated for an idealized situation for simplicity, shows that the $\tau$-derivative of the cross-correlation is a smoothed and symmetrized version of the Green's function.

PROPOSITION 1. *Consider an inhomogeneous cavity with homogeneous dissipation quantified by $1/T_a$. Suppose that the source distribution extends over the whole cavity, i.e., $K(\boldsymbol{y}) = \mathbf{1}_\Omega(\boldsymbol{y})$ in* (4.1). *Then, for any $r,r' = 1,\dots,m$, we have*

$$\partial_\tau C^{(1)}(\tau,\boldsymbol{x}_r,\boldsymbol{x}_{r'}) = -\frac{T_a}{4}F(\tau)\star_\tau\big[\mathrm{sgn}(\tau)G(|\tau|,\boldsymbol{x}_r,\boldsymbol{x}_{r'})\big], \tag{4.5}$$

*where $G$ is the Green's function* (4.3) *and* $\mathrm{sgn}(t) = H(t) - H(-t)$ *is the sign function.*

The proof can be found in [42, section 2.5]. Note that $C^{(1)}$ is an even function in $\tau$, and therefore its $\tau$-derivative is an odd function.

We can now give the relationship between the cross-correlation matrix and the data matrix $\boldsymbol{D}(t)$ exploited in the ROM procedure.

THEOREM 4. *We have, for any $r,r' = 1,\dots,m$, that*

$$\frac{1}{T_a}\partial_\tau^2 C^{(1)}(\tau,\boldsymbol{x}_r,\boldsymbol{x}_{r'}) \overset{T_a\to+\infty}{\longrightarrow} -\frac{1}{4}D_{r,r'}(\tau), \tag{4.6}$$

*where $\boldsymbol{D}(t)$ is the matrix defined in Lemma* 1 *with a signal $f(t)$ whose Fourier transform satisfies $|\widehat{f}(\omega)| = \widehat{F}^{\frac{1}{2}}(\omega)$.*

*Proof.* From Proposition 1 we obtain

$$\frac{1}{T_a}\partial_\tau^2 C^{(1)}(\tau,\boldsymbol{x}_r,\boldsymbol{x}_{r'}) \overset{T_a\to+\infty}{\longrightarrow} -\frac{1}{4}\sum_{j=1}^{\infty}\int_{\mathbb{R}} dt\, F(\tau-t)\cos\big(\sqrt{\theta_j}t\big)\, y_j(\boldsymbol{x}_r)y_j(\boldsymbol{x}_{r'}),$$

where

$$\int_{\mathbb{R}} dt\, F(\tau-t)\cos(\sqrt{\theta_j}t) = \int_{\mathbb{R}} d\omega\, \widehat{F}(\omega)e^{i\omega\tau}\int_{\mathbb{R}}\frac{dt}{2\pi}\cos(\sqrt{\theta_j}t)e^{i\omega t} = \widehat{F}(\sqrt{\theta_j})\cos(\sqrt{\theta_j}\tau).$$

We obtain the desired result after deducing from (2.9) and (2.11) that

$$D_{r,r'}(\tau) = \sum_{j=1}^{\infty}\widehat{F}(\sqrt{\theta_j})\cos(\sqrt{\theta_j}\tau)y_j(\boldsymbol{x}_r)y_j(\boldsymbol{x}_{r'}). \qquad \square$$

Theorem 4 says that we can approximate $\boldsymbol{D}(t)$ for weak attenuation, i.e., $\tau \ll T_a$. It shows that our ROM procedure is natural in the passive framework, since the cross-correlation of the noise signals recorded by an array of receivers gives the data matrix $\boldsymbol{D}(t)$ corresponding to a virtual active array directly. The virtual sources and receivers are naturally colocated and the signals are even, because the cross-correlations are even, thus circumventing the transformation in Lemma 1.

REMARK 4.1. *Here we considered a cavity $\Omega$ with uniformly distributed noise sources in $\Omega$. In this idealized case, no hypothesis regarding the geometry of the cavity is needed to obtain the result in Proposition* 1. *However, this result also holds when the noise source distribution is nonhomogeneous or spatially limited, provided the cavity possesses some ergodic properties and the attenuation time $T_a$ is larger than the critical time necessary to reach ergodicity* [7, 28].

**5. Concluding Remarks and Open Questions.** Our goal in this paper was to show how computationally efficient tools from numerical linear algebra and reduced order modeling can be used to improve the existing inverse scattering methodology. We presented in a unified way two projection-type ROMs that capture wave propagation in complementary ways and have the following important properties for solving waveform inversion problems: (1) They can be computed from measurements of the waves that are available in most application setups. These include data acquisitions with controlled sources that emit probing pulses and unconventional ones with uncontrolled noise sources. (2) The mapping from the data to the ROMs is nonlinear and yet the ROM computation can be carried out with known linear algebra algorithms, in a noniterative fashion. (3) This computation can be done such that the causal physics of wave propagation is captured by a special algebraic structure of the ROM matrices. This is essential for the success of the inversion.

We described two ideas for using the ROMs for inversion that are quite a departure from the data fitting approaches found in the literature. The inversion results based on the ROMs are promising, but the methodology is young and there are many open questions. Here are a few examples:

1. The dependence of the projection basis $\boldsymbol{V}(\boldsymbol{x})$ on $c(\boldsymbol{x})$ is understood only in a few media [19, Appendix A]. This basis also depends on the choice of $\tau$ and the separation between the sensors in the array. A deeper understanding of $\boldsymbol{V}(\boldsymbol{x})$ would lead to a more rigorous foundation of waveform inversion based on $\mathcal{A}^{\text{ROM}}$ and of ROM based imaging methods like [19, 33, 16].

2. How can one extend the ROM methodology to setups where the sources are still controlled by the user, but are placed in different locations than those of the receivers? The gathered data matrices are no longer symmetric in such cases and a different projection methodology of the Petrov–Galerkin type should be used. It is not difficult to find ROMs that do a good job in terms of approximating the forward map in such settings. However, it is not yet known how to find ROMs that are useful for inversion.

3. The proposed ROM construction relies on having a self-adjoint wave operator, which is no longer the case if there is attenuation. If the attenuation coefficient $T_a$ is constant and known, as assumed in section 4, then it is possible to remove attenuation effects by multiplying the measurements with $\exp(t/T_a)$. This is feasible if the attenuation is weak. The case of variable attenuation requires a fundamental rethinking of the methodology, as does the case of dispersive media.

4. The ROM based inversion methodology extends to media with variable mass density, to anisotropic media, and to electromagnetic waves. Inversion with elastic

waves remains largely unexplored. The main difficulty in that case is due to the multiple wave modes that propagate at different wave speeds.

We hope that this paper will motivate the applied and computational mathematics community to explore this new way of solving inverse wave scattering problems.

**Appendix A. Setup for the Numerical Simulations.** All the simulations performed are in a two-dimensional rectangular domain with sound soft boundary. The data are computed with a time-domain solver for the wave equation (1.1) with a five point stencil discretization of the Laplacian on a uniform grid and a three point finite difference scheme for the second time derivative. The spatial mesh size is 20m for Figure 3.4, 18.75m for Figure 3.5, and 25m for Figure 3.6 and the time grid step is $\Delta t = \tau/20$.

The data matrices are computed using definition (2.3). To compute the second derivative data matrices, we extend the finely sampled data evenly in discrete time to get $\boldsymbol{D}_{e,j}$, with $\boldsymbol{D}_j = \boldsymbol{D}_{e,\pm j}$, for $j = 0, 1, \ldots, N$. Then, we take the discrete Fourier transform of $(\boldsymbol{D}_{e,j})_{j=-N}^{N}$ and differentiate in the Fourier domain after using a sharp cutoff low-pass filter intended to stabilize the calculation. The cutoff frequency is at $(\omega_o + 4B)/(2\pi)$. We take the inverse Fourier transform to obtain $\ddot{\boldsymbol{D}}_{e,j}$ at $j = -N, \ldots, N$. Finally, we subsample $\boldsymbol{D}_{e,j}$ and $\ddot{\boldsymbol{D}}_{e,j}$ to get $\boldsymbol{D}_j = \boldsymbol{D}_{e,20j}$ and $\ddot{\boldsymbol{D}}_j = \ddot{\boldsymbol{D}}_{e,20j}$ for $j = 0, 1, \ldots, 2n-1$.

All the simulations use the probing signal $f(t) = B\exp(-B^2t^2/2)\cos(\omega_o t)$, with $\omega_o/(2\pi) = 6$Hz and $B/(2\pi) = 4$Hz. The array of $m$ colocated sensors (sources and receivers) with aperture $a$ is near the top boundary, at a depth equal to the central wavelength. The parameters for the experiments in Figures 3.4–3.6 are in Table A.1.

**Table A.1** *Numerical parameters for the experiments in Figures* 3.4–3.6.

| Fig. | $\Omega$ (km) | $\Omega_{\text{inv}}$ (m) | $\bar{c}$ (km/s) | $\lambda_o$ (m) | $m$ | $a$ (m) | $\tau$ (s) | $n$ | $N_t$ | $N$ | $\sigma^{\perp}$ (m) | $\sigma$ (m) |
|---|---|---|---|---|---|---|---|---|---|---|---|---|
| 3.4 | $[0,2]\times$ $[0,2.5]$ | $[95,1905]\times$ $[119,2381]$ | 3 | 300 | 10 | 1400 | 0.0435 | 16 | 6 | 400 | 55.5 | 69.4 |
| 3.5 | $[0,6]\times$ $[0,5.25]$ | $[105,5895]\times$ $[92,5158]$ | 1.5 | 150 | 40 | 5550 | 0.0333 | 49 | 6 | 3025 | 61.2 | 53.6 |
| 3.6 | $[0,6.5]\times$ $[0,6.5]$ | $[114,6386]\times$ $[300,6392]$ | 1.5 | 150 | 40 | 4500 | 0.05 | 86 | 9 | 3025 | 66.6 | 63.4 |

**Acknowledgments.** We thank Vladimir Druskin, Mike Zaslavsky, and Andy Thaler for their foundational work on the data driven ROM methodology.

## REFERENCES

[1] D. G. Alfaro Vigo, J.-P. Fouque, J. Garnier, and A. Nachbin, *Robustness of time reversal for waves in time-dependent random media*, Stochastic Process. Appl., 113 (2004), pp. 289–313. (Cited on p. 524)

[2] A. Antoulas, D. Sorensen, and S. Gugercin, *A survey of model reduction methods for large-scale systems*, Contemp. Math., 280 (2001), pp. 193–220. (Cited on p. 505)

[3] S. Arridge and O. Scherzer, *Imaging from coupled physics*, Inverse Problems, 28 (2012), art. 080201. (Cited on p. 517)

[4] S. Asvadurov, V. Druskin, M. N. Guddati, and L. Knizhnerman, *On optimal finite-difference approximation of PML*, SIAM J. Numer. Anal., 41 (2003), pp. 287–305, https://doi.org/10.1137/S0036142901391451. (Cited on p. 507)

[5] G. Bal and G. Uhlmann, *Reconstruction of coefficients in scalar second-order elliptic equations from knowledge of their solutions*, Comm. Pure Appl. Math., 66 (2013), pp. 1629–1652. (Cited on p. 517)

[6] G. Bal and R. Verástegui, *Time reversal in changing environments*, Multiscale Model. Simul., 2 (2004), pp. 639–661, https://doi.org/10.1137/030600837. (Cited on p. 524)
[7] C. Bardos, J. Garnier, and G. Papanicolaou, *Identification of Green's functions singularities by cross correlation of noisy signals*, Inverse Problems, 24 (2008), art. 015011. (Cited on p. 528)
[8] M. Belishev, *Recent progress in the boundary control method*, Inverse Problems, 23 (2007), art. R1. (Cited on p. 503)
[9] P. Benner, S. Gugercin, and K. Willcox, *A survey of projection-based model reduction methods for parametric dynamical systems*, SIAM Rev., 57 (2015), pp. 483–531, https://doi.org/10.1137/130932715. (Cited on pp. 505, 515)
[10] F. Billette and S. Brandsberg-Dahl, *The* 2004 *BP velocity benchmark*, in 67th Annual EAGE Meeting, Expanded Abstracts, European Association of Geoscientists & Engineers, 2005, art. cp-1-00513. (Cited on p. 523)
[11] N. Bleistein, J. Stockwell, and J. Cohen, *Multidimensional Seismic Inversion*, Springer, 2001. (Cited on pp. 503, 505)
[12] L. Borcea, V. Druskin, and F. Guevara-Vasquez, *Electrical impedance tomography with resistor networks*, Inverse Problems, 24 (2008), art. 035013. (Cited on p. 507)
[13] L. Borcea, V. Druskin, and L. Knizhnerman, *On the continuum limit of a discrete inverse spectral problem on optimal finite difference grids*, Comm. Pure Appl. Math., 58 (2005), pp. 1231–1279. (Cited on p. 507)
[14] L. Borcea, V. Druskin, and A. Mamonov, *Circular resistor networks for electrical impedance tomography with partial boundary measurements*, Inverse Problems, 26 (2010), art. 045010. (Cited on p. 507)
[15] L. Borcea, V. Druskin, A. V. Mamonov, and M. Zaslavsky, *A model reduction approach to numerical inversion for a parabolic partial differential equation*, Inverse Problems, 30 (2014), art. 125011. (Cited on p. 526)
[16] L. Borcea, V. Druskin, A. V. Mamonov, and M. Zaslavsky, *Untangling the nonlinearity in inverse scattering with data-driven reduced order models*, Inverse Problems, 34 (2018), art. 065008. (Cited on pp. 507, 517, 520, 528)
[17] L. Borcea, V. Druskin, A. V. Mamonov, and M. Zaslavsky, *Robust nonlinear processing of active array data in inverse scattering via truncated reduced order models*, J. Comput. Phys., 381 (2019), pp. 1–26. (Cited on p. 507)
[18] L. Borcea, V. Druskin, A. V. Mamonov, M. Zaslavsky, and J. Zimmerling, *Reduced order model approach to inverse scattering*, SIAM J. Imaging Sci., 13 (2020), pp. 685–723, https://doi.org/10.1137/19M1296355. (Cited on pp. 507, 508, 515)
[19] L. Borcea, J. Garnier, A. Mamonov, and J. Zimmerling, *Reduced order model approach for imaging with waves*, Inverse Problems, 38 (2021), art. 025004. (Cited on pp. 509, 517, 528)
[20] L. Borcea, J. Garnier, A. Mamonov, and J. Zimmerling, *Waveform inversion via reduced order modeling*, Geophys., 88 (2022), pp. 1–91. (Cited on pp. 506, 507, 509, 510, 515, 516, 517, 520, 521, 523, 526)
[21] L. Borcea, J. Garnier, A. V. Mamonov, and J. Zimmerling, *Waveform inversion with a data driven estimate of the internal wave*, SIAM J. Imaging Sci., 16 (2023), pp. 280–312, https://doi.org/10.1137/22M1517342. (Cited on pp. 507, 509, 519, 523)
[22] C. Borges, A. Gillman, and L. Greengard, *High resolution inverse scattering in two dimensions using recursive linearization*, SIAM J. Imaging Sci., 10 (2017), pp. 641–664, https://doi.org/10.1137/16M1093562. (Cited on p. 505)
[23] S. Brunton and J. Kutz, *Data-Driven Science and Engineering: Machine Learning, Dynamical Systems, and Control*, Cambridge University Press, 2019. (Cited on p. 506)
[24] S. Brunton, J. Proctor, and J. Kutz, *Discovering governing equations from data by sparse identification of nonlinear dynamical systems*, Proc. Natl. Acad. Sci. USA, 113 (2016), pp. 3932–3937. (Cited on p. 506)
[25] C. Bunks, F. Saleck, S. Zaleski, and G. Chavent, *Multiscale seismic waveform inversion*, Geophys., 60 (1995), pp. 1457–1473. (Cited on p. 505)
[26] Y. Chen, *Inverse scattering via Heisenberg's uncertainty principle*, Inverse Problems, 13 (1997), pp. 253–282. (Cited on p. 505)
[27] M. Cheney and B. Borden, *Fundamentals of Radar Imaging*, SIAM, 2009, https://doi.org/10.1137/1.9780898719291. (Cited on p. 503)
[28] Y. Colin de Verdière, *Semiclassical analysis and passive imaging*, Nonlinearity, 22 (2009), pp. R45–R75. (Cited on p. 528)
[29] G. Côrte, J. Dramsch, H. Amini, and C. MacBeth, *Deep neural network application for 4D seismic inversion to changes in pressure and saturation: Optimizing the use of synthetic*

*training datasets*, Geophys. Prospecting, 68 (2020), pp. 2164–2185. (Cited on p. 505)
[30] J. Curlander and R. McDonough, *Synthetic Aperture Radar*, Vol. 11, Wiley, 1991. (Cited on p. 503)
[31] W. Ding, K. Ren, and L. Zhang, *Coupling Deep Learning with Full Waveform Inversion*, preprint, https://arxiv.org/abs/2203.01799, 2022. (Cited on p. 505)
[32] V. Druskin, A. V. Mamonov, A. E. Thaler, and M. Zaslavsky, *Direct, nonlinear inversion algorithm for hyperbolic problems via projection-based model reduction*, SIAM J. Imaging Sci., 9 (2016), pp. 684–747, https://doi.org/10.1137/15M1039432. (Cited on p. 507)
[33] V. Druskin, A. V. Mamonov, and M. Zaslavsky, *A nonlinear method for imaging with acoustic waves via reduced order model backprojection*, SIAM J. Imaging Sci., 11 (2018), pp. 164–196, https://doi.org/10.1137/17M1133580. (Cited on pp. 507, 517, 528)
[34] V. Druskin and S. Moskow, *Three-point finite-difference schemes, Padé and the spectral Galerkin method.* I. *One-sided impedance approximation*, Math. Comp., 71 (2002), pp. 995–1019. (Cited on p. 507)
[35] B. Engquist and B. Froese, *Application of the Wasserstein metric to seismic signals*, Commun. Math. Sci., 12 (2014), pp. 979–988. (Cited on pp. 505, 522)
[36] B. Engquist and Y. Yang, *Optimal transport based seismic inversion: Beyond cycle skipping*, Comm. Pure Appl. Math., 75 (2022), pp. 2201–2244. (Cited on p. 505)
[37] M. Fink, *Time-reversed acoustics*, Sci. Amer., 281 (1999), pp. 91–97. (Cited on p. 524)
[38] J.-P. Fouque, J. Garnier, G. Papanicolaou, and K. Sølna, *Wave Propagation and Time Reversal in Randomly Layered Media*, Springer, New York, 2007. (Cited on p. 524)
[39] J. Garnier, *Passive communication with ambient noise*, SIAM J. Appl. Math., 81 (2021), pp. 814–833, https://doi.org/10.1137/20M1366848. (Cited on p. 526)
[40] J. Garnier and G. Papanicolaou, *Passive sensor imaging using cross correlations of noisy signals in a scattering medium*, SIAM J. Imaging Sci., 2 (2009), pp. 396–437, https://doi.org/10.1137/080723454. (Cited on p. 526)
[41] J. Garnier and G. Papanicolaou, *Resolution analysis for imaging with noise*, Inverse Problems, 26 (2010), art. 074001. (Cited on p. 526)
[42] J. Garnier and G. Papanicolaou, *Passive Imaging with Ambient Noise*, Cambridge University Press, 2016. (Cited on pp. 506, 526, 527)
[43] O. Gauthier, J. Virieux, and A. Tarantola, *Two-dimensional nonlinear inversion of seismic waveforms: Numerical results*, Geophys., 51 (1986), pp. 1387–1403. (Cited on p. 522)
[44] P. E. Gill, W. Murray, and M. H. Wright, *Practical Optimization*, SIAM, 2019, https://doi.org/10.1137/1.9781611975604. (Cited on p. 504)
[45] M. Gilman, E. Smith, and S. Tsynkov, *Transionospheric Synthetic Aperture Imaging*, Birkhäuser, Cham, 2017. (Cited on p. 503)
[46] G. H. Golub and C. F. Van Loan, *Matrix Computations*, Johns Hopkins University Press, Baltimore, MD, 2013. (Cited on p. 516)
[47] S. Herkt, M. Hinze, and R. Pinnau, *Convergence analysis of Galerkin POD for linear second order evolution equations*, Electron. Trans. Numer. Anal., 40 (2013), pp. 321–337. (Cited on p. 506)
[48] J. Hesthaven, C. Pagliantini, and G. Rozza, *Reduced basis methods for time-dependent problems*, Acta Numer., 31 (2022), pp. 265–345. (Cited on pp. 506, 515)
[49] G. Huang, R. Nammour, and W. Symes, *Source-independent extended waveform inversion based on space-time source extension: Frequency-domain implementation*, Geophys., 83 (2018), pp. R449–R461. (Cited on p. 505)
[50] O. Imanuvilov and M. Yamamoto, *Global uniqueness and stability in determining coefficients of wave equations*, Comm. Partial Differential Equations, 26 (2001), pp. 1409–1425. (Cited on p. 503)
[51] I. Jollife and J. Cadima, *Principal component analysis: A review and recent developments*, Philos. Trans. Roy. Soc. A, 374 (2016), art. 20150202. (Cited on p. 515)
[52] K. Karhunen, *Über lineare Methoden in der Wahrscheinlichkeitsrechnung*, Ann. Acad. Sci. Fennicae Ser. A. I. Math.-Phys., 37 (1947), pp. 1–79. (Cited on p. 515)
[53] T. Kato, *Perturbation Theory for Linear Operators*, Grundlehren Math. Wiss. 132, Springer, 2013. (Cited on p. 508)
[54] K. Kunisch and S. Volkwein, *Optimal snapshot location for computing POD basis functions*, M2AN Math. Model. Numer. Anal., 44 (2010), pp. 509–529. (Cited on p. 506)
[55] T. Lieu, C. Farhat, and M. Lesoinne, *Reduced-order fluid/structure modeling of a complete aircraft configuration*, Computer Methods Appl. Mech. Engrg., 195 (2006), pp. 5730–5742. (Cited on pp. 506, 515)
[56] O. I. Lobkis and R. L. Weaver, *On the emergence of the Green's function in the correlations of a diffuse field*, J. Acoust. Soc. Amer., 110 (2001), pp. 3011–3017. (Cited on p. 526)

[57] M. Loeve, *Probability Theory*, Vol. II, 4th ed., Springer-Verlag, 1978. (Cited on p. 515)
[58] S. Mahankali and Y. Yang, *The Convexity of Optimal Transport-Based Waveform Inversion for Certain Structured Velocity Models*, preprint, https://arxiv.org/abs/2009.00708, 2020. (Cited on p. 505)
[59] A. Nachman, A. Tamasan, and A. Timonov, *Conductivity imaging with a single measurement of boundary and interior data*, Inverse Problems, 23 (2007), pp. 2551–2563. (Cited on p. 517)
[60] W. Schilders, H. Van der Vorst, and J. Rommes, *Model Order Reduction: Theory, Research Aspects and Applications*, Math. Induct. 13, Springer, 2008. (Cited on p. 505)
[61] P. Stefanov and G. Uhlmann, *Stable determination of generic simple metrics from the hyperbolic Dirichlet-to-Neumann map*, Int. Math. Res. Not., 2005 (2005), pp. 1047–1061. (Cited on p. 503)
[62] W. Symes, *Migration velocity analysis and waveform inversion*, Geophys. Prospecting, 56 (2008), pp. 765–790. (Cited on pp. 505, 525)
[63] W. Symes, *Error bounds for extended source inversion applied to an acoustic transmission inverse problem*, Inverse Problems, 38 (2022), art. 115002. (Cited on p. 505)
[64] T. van Leeuwen and F. Herrmann, *Mitigating local minima in full-waveform inversion by expanding the search space*, Geophys. J. Internat., 195 (2013), pp. 661–667. (Cited on p. 505)
[65] J. Virieux and S. Operto, *An overview of full-waveform inversion in exploration geophysics*, Geophys., 74 (2009), pp. WCC1–WCC26. (Cited on pp. 504, 505, 525)
[66] M. Warner and L. Guasch, *Adaptive waveform inversion: Theory*, Geophys., 81 (2016), pp. R429–R445. (Cited on p. 505)
[67] Y. Yang, B. Engquist, J. Sun, and B. Hamfeldt, *Application of optimal transport and the quadratic Wasserstein metric to full-waveform inversion*, Geophys., 83 (2018), pp. R43–R62. (Cited on p. 505)